nature communications

Article

https://doi.org/10.1038/s41467-024-51149-4

Transcription-dependent mobility of single genes and genome-wide motions in live human cells

Received: 22 April 2020

Accepted: 31 July 2024

Published online: 22 October 2024

Check for updates

Fang-Yi Chu[1,2], Alexis S. Clavijo[1,2], Suho Lee[1] & Alexandra Zidovska[1]

The human genome is highly dynamic across all scales. At the gene level, chromatin is persistently remodeled and rearranged during active processes such as transcription, replication and DNA repair. At the genome level, chromatin moves in micron-scale domains that break up and re-form over seconds, but the origin of these coherent motions is unknown. Here, we investigate the connection between genomic motions and gene-level activity. Simultaneous mapping of single-gene and genome-wide motions shows that the coupling of gene transcriptional activity to flows of the nearby genome is modulated by chromatin compaction. A motion correlation analysis suggests that a single active gene drives larger-scale motions in low-compaction regions, but high-compaction chromatin drives gene motion regardless of its activity state. By revealing unexpected connections among gene activity, spatial heterogeneities of chromatin and its emergent genome-wide motions, these findings uncover aspects of the genome's spatiotemporal organization that directly impact gene regulation and expression.

The spatio-temporal organizaton of the human genome plays a key role in all cellular processes, directly affecting the central dogma of biology[1,2]. While the static folding of the human genome has been revealed by chromosome conformation capture techniques[3–5], it remains unclear how it evolves over time, especially at large length scales[6–8]. The mapping of real-time genome dynamics across an entire nucleus in live cells was recently accomplished by the displacement correlation spectroscopy (DCS)[9]. DCS uncovered that interphase chromatin exhibits two types of motion in the cell nucleus: a fast, local motion, consistent with single particle tracking studies[10–18], and a slow, coherent motion, where micron-scale regions (3–5 μm) of chromatin move together for several seconds[9]. These two types of motion occur in the nucleus concurrently and superposed. The coherent motion has major implications for dynamical self-organization of the genome, enabling groups of genes to travel together for several seconds, although its biological function as well as the underlying biophysical mechanism(s) remain open questions.

Chromatin undergoes frequent local remodeling and rearrangements to accommodate processes such as transcription, replication and DNA repair[19–21]. How these local activities contribute to nucleus-wide coherent chromatin motion, is unknown. The coherent motions were found to be ATP-dependent, but independent of cytoskeletal activity[9]. To elucidate the biophysical origins of the coherent motion, nuclear ATPases driving the coherent motion need to be identified. Interestingly, blocking the activity of polymerase II, helicase and topoisomerase led to an elimination of the coherent motion and increase in the local chromatin displacements[9,22]. However, these inhibitions induce a DNA damage response, dynamics of which obscures the changes in chromatin motion due to the blocked molecular motors[9]. Motivated by the DCS measurements, a hydrodynamic theory of active chromatin dynamics was developed[23], which predicts an active process represented by a force dipole (a pair of opposite forces of an equal magnitude) to drive the coherent motion[23]. Moreover, numerical simulations of a hydrodynamically self-interacting chromatin fiber with dipolar activity acting on it, identified extensile (outward) force dipoles as essential for generating coherent motion[24]. Hydrodynamics-free approaches also recapitulated coherent motion in the presence of activity on the chromatin fiber[25–27].

[1]Center for Soft Matter Research, Department of Physics, New York University, New York, NY 10003, USA. [2]These authors contributed equally: Fang-Yi Chu, Alexis S. Clavijo. e-mail: alexandra.zidovska@nyu.edu

Many active processes, such as transcription, replication, chromatin remodeling or DNA repair, might be contributing to the coherent motion. Notably, some of them take place only in specific cell cycle stages (e.g., replication in S-phase), while transcription occurs during the entire interphase[28]. For example, in HeLa cells ~60% of the genome becomes expressed during their lifetime, with ~14% being actively transcribed at any given time[29–31]. Moreover, mobility of single genes was shown to change upon their transcriptional activation, with some genes showing reduced, some enhanced local motion[16,32–35]. Similarly, chromatin surrounding active genes was found to change when genes were activated, in some cases increasing, in some cases reducing the constraint on the gene motion[32,36–38]. The high heterogeneity of chromatin density and packing across the nuclear interior has been shown to give rise to differences in local material properties of chromatin[39]. Hence, the motion of the genes may depend not only on their transcriptional activity, but also on the material properties of their local physical environment. A dysfunction or misregulation of transcription leads to diseases including neurological and cardiovascular disorders, as well as cancer[40,41]. Thus, understanding mechanics behind transcription-dependent motions of single genes in the nucleus might be critical for understanding the genome dynamics in health and disease.

In this work, we study the dynamical contribution of a single gene transcription to the large-scale genomic motion in living cells (Fig. 1a). Using simultaneous two-color spinning disc confocal microscopy, we map nucleus-wide chromatin dynamics by DCS, while at the same time visualizing single gene motion by CRISPR-dCas9-PCP-mCherry system (see *Methods*). We monitor behavior of two genes, *MUC4* and *IL6*, with repetitive and non-repetitive sequence, respectively, as a function of their transcriptional activity and compaction of their chromatin environment.

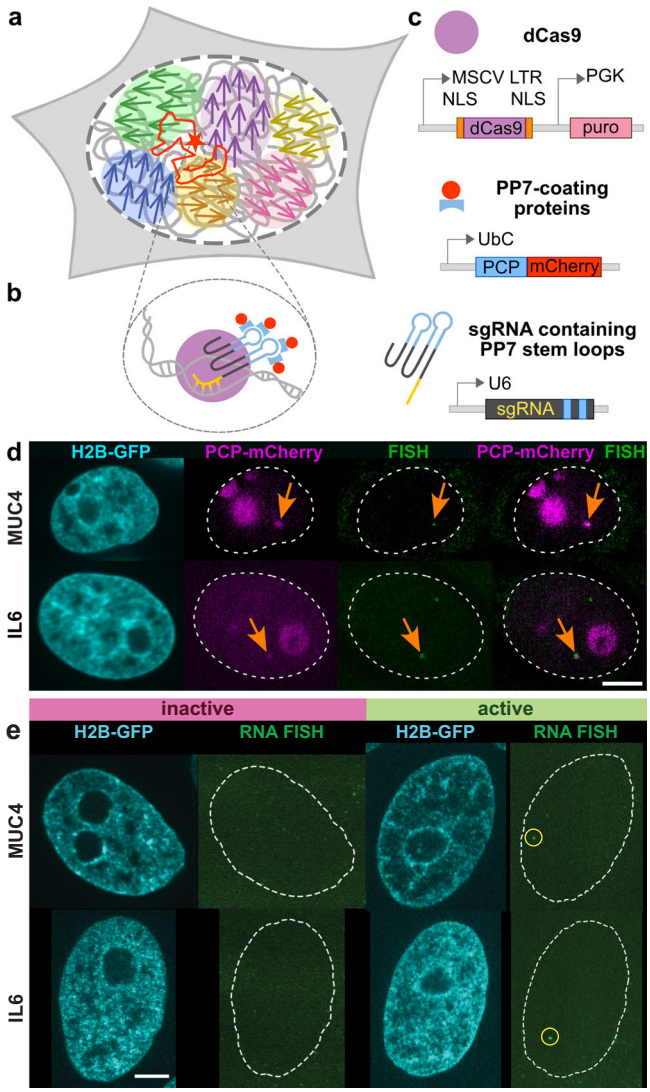

Fig. 1 | In vivo visualization of single genes using CRISPR-dCas9 and PP7 stem-loop binding proteins. a Cartoon of a gene (red star) and its trajectory (red line) surrounded by coherently moving chromatin regions (arrows). **b** The inset shows an illustration of a gene labeled by CRISPR-dCas9 and PP7 stem-loop binding proteins. Adapted from[42]. **c** Schematics of the used constructs: dCas9 protein with two nuclear localization signals (NLS), PP7 stem-loop binding proteins (PCP) tagged with mCherry, and target-specific sgRNA scaffolds, each containing two PP7 stem loops. Adapted from[42]. **d** Visualization of *MUC4* and *IL6* using CRISPR-dCas9-PCP-mCherry system in HeLa cells in vivo: Chromatin is visualized by H2B-GFP (cyan) and *MUC4*/*IL6* position by CRISPR-dCas9-PCP-mCherry (magenta). The *MUC4*/*IL6* positions are verified using gene-specific FISH labeling (green). An overlay of magenta and green signals shows a co-localization of the puncta in the two signals (highlighted by orange arrows). **e** Micrographs of transcriptionally unstimulated (inactive) and stimulated (active) nuclei with fluorescently labeled H2B-GFP (cyan) and nascent RNA at *IL6*/*MUC4* labeled by RNA FISH (green). RNA FISH probe location is highlighted by yellow circles. All images correspond to a single focal plane. Scale bar, 5 μm.

Results

Visualization of active and inactive genes in vivo

To simultaneously visualize and interrogate dynamics of a single gene and its surrounding chromatin in vivo (Fig. 1a), we created a transgenic HeLa cell line stably expressing both the cleavage-deficient Cas9 (dCas9) and histone H2B-GFP (see *Methods* for detailed protocols). These cells were then simultaneously transfected with sequence-specific single-guide RNAs (sgRNAs), which contain two PP7 RNAs stem loops, and PCP-mCherry, a fluorescently labeled PP7 coat protein, which binds to PP7 RNA loops, following procedures in[42] (Fig. 1b-c). To validate this approach, we first imaged telomeres, known for their repetitive sequence, using previously published sgRNA design containing 22 nucleotide target sequence with PP7 loops[14]. Employing this approach we successfully obtained the characteristic punctate signal for telomeres, whose correct localization we confirmed by telomere-specific peptide nucleic acid (PNA) fluorescence in situ hybridization (FISH) (Supplementary Fig. 1).

To investigate the dynamics of a single gene undergoing transcription, we chose to study genes *MUC4* (65 kb) and *IL6* (5 kb), which are part of the immune response in HeLa cells[43,44]. *MUC4* encodes for a glycoprotein, which constitutes mucus on the epithelial cell layers, and *IL6* encodes for an interleukin, which acts as a pro-inflammatory cytokine[43,45]. While *MUC4* has a repetitive sequence requiring a single sgRNA for its visualization in vivo using the CRISPR-dCas9-PCP-mCherry approach, *IL6* has a non-repetitive sequence, which necessitated a design of 67 unique sgRNAs (see *Methods*). Figure 1d shows nuclei with fluorescently labeled chromatin (H2B-GFP, cyan) and the positions of *MUC4* and *IL6*, respectively, determined by the CRISPR-dCas9-PCP-mCherry signal (PCP-mCherry, magenta). Signal-to-noise ratio of detected gene loci is shown in Supplementary Fig. 2a. We verified the specificity of the CRISPR-dCas9-PCP-mCherry signal (Fig. 1d, magenta) by showing its co-localization with the respective gene sequence visualized by FISH using human BAC clones for *MUC4* and *IL6*, respectively (Fig. 1d, green).

MUC4 and *IL6* are initially transcriptionally inactive in HeLa cells, but can be activated by inflammatory stimuli such as IFNγ and TNFα for *MUC4*[46], and lipopolysaccharide (LPS) for *IL6*[47,48]. We activated transcription of *MUC4* and *IL6* using these respective stimuli. To verify the transcription activation of *MUC4*/*IL6*, we visualized nascent RNA at *MUC4*/*IL6* using RNA FISH (see *Methods*). We find foci of nascent RNA at *MUC4*/*IL6* in transcriptionally stimulated (active) nuclei, but never in unstimulated (inactive) nuclei (Fig. 1e). Specifically, we found 102 RNA

foci across 72 *IL6*-stimulated nuclei and 48 RNA foci across 37 *MUC4*-stimulated nuclei, while we detected no RNA foci across 30 *IL6*-unstimulated nuclei and 30 *MUC4*-unstimulated nuclei. Signal-to-noise ratio of the detected RNA FISH foci was consistent with earlier studies[49](Supplementary Fig. 2b). Considering that transcriptional bursts have a duration of ~10–100 min, with time of inactivity between bursts of ~100 min[50,51], we could be randomly sampling active genes bursting or in between bursts. Given our observed RNA foci counts and the HeLa cell ploidy[52] (we expect 3 copies of both genes per nucleus), we can estimate that at least 47% of *IL6* and 43% of *MUC4* genes are actively transcribing at the time of observation. With the mRNA splicing times ~15 s–5 min[53] and the degradation half-life of spliced introns ~5 min[54], the detected RNA FISH foci point to an ongoing transcriptional activity. Our estimates present a lower bound, as some mRNA targets may be lost (e.g. washed away) during the fixation procedure. In addition, stimulated genes are subject to forms of activity beyond the transcription itself, e.g. remodeling pre/post transcription[55].

To monitor production of nascent RNA at active *MUC4*/*IL6* as a function of time, we performed RNA FISH at different time points up to 3 hrs after the transcriptional stimulation and observed no significant changes in the encounter frequency of RNA FISH foci (Supplementary Fig. 3). In addition, we visualized transcriptionally active RNA polymerase II (RNA pol II with phosphorylated S5 CTD) in control cells and transcriptionally stimulated cells using immunofluorescence. We observe a co-localization of *MUC4*/*IL6* genes with active RNA pol II only upon their transcriptional activation (Supplementary Fig. 4). However, the colocalization of the two signals in the active case is not a definitive evidence of the gene activation, since active genes in close proximity (below optical resolution) would also yield RNA pol II signal. Hence, the definitive evidence is provided in Fig. 1e, where we show the sequence-specific RNA FISH imaging for both *MUC4* and *IL6*.

Transcriptional stimulation of *MUC4*/*IL6* could also lead to activation of other genes. To assess any potential changes in the overall gene activity upon the two studied stimuli, we measure the density of active genes in the nucleus before and after LSP/IFNγ + TNFα stimulation (Supplementary Fig. 5a). Specifically, we count the number of active RNA pol II foci in a focal plane, which we normalize by the nuclear area in the given plane, and find the average active RNA pol II density of 0.92 ± 0.09 foci/μm^2 over 94 unstimulated nuclei, 0.94 ± 0.09 foci/μm^2 over 67 *IL6* stimulated nuclei, and 0.97 ± 0.07 foci/μm^{2}over 67 *MUC4* stimulated nuclei (mean ± standard deviation, Supplementary Fig. 5b). Our data show, there are no significant changes in the overall gene activity upon the two studied stimuli. It is important to note that we apply LPS only for 30 min. Our observations are consistent with an earlier study showing minimal changes in overall transcriptional activity after 1 h LPS stimulation[56]. Thus, our approach allows for visualization of *MUC4*/*IL6* genes in vivo, while controlling for their respective transcriptional activity at a local level.

Single gene vs. large scale chromatin dynamics

To monitor the transcription-dependent motion of *MUC4* and *IL6* (CRISPR-dCas9-PCP-mCherry), while observing dynamics of their surrounding chromatin (H2B-GFP), we used simultaneous two-color spinning disc confocal microscopy allowing us to record both signals, CRISPR-dCas9-PCP-mCherry and H2B-GFP at the same time (see *Methods* and Supplementary Movies 1–2). Specifically, we recorded high-resolution streams (~65 nm pixel size in x and y, 250 ms per frame) for both signals for 20 s before and after the transcription activation of *MUC4* and *IL6* (Fig. 2a). Using single particle tracking (SPT), we follow the *MUC4*/*IL6* motion in their respective CRISPR-dCas9-PCP-mCherry signals and obtain trajectories for all tracked genes (Fig. 2b, see *Methods* and Supplementary Movie 3). In addition, we analyze the H2B-GFP signal by Displacement Correlation Spectroscopy (DCS)[9], which maps chromatin motion across the entire nucleus in real time (see *Methods*). DCS measures chromatin motion over time intervals Δt, sampling over all time intervals, i.e., timescales, accessible by the experiment. We obtain the DCS maps for $\Delta t = 0.25 - 15$ s: Fig. 2c and d show examples of DCS maps at $\Delta t = 0.25$ s and $\Delta t = 10$ s, respectively (Supplementary Movies 4–5). The displacement vectors are color-coded by their direction, i.e., vectors of the same color point into the same direction.

Consistent with earlier studies[9], at short time intervals chromatin displacements are uncorrelated (Fig. 2c and Supplementary Fig. 6b), while at longer time intervals chromatin displacements become correlated over few microns (Fig. 2d and Supplementary Fig. 6c). To quantify the extent of displacement correlation at different Δt, we compute the spatial autocorrelation function $C_{d_x}(\Delta\mathbf{r},\Delta t) = \langle d_x(\mathbf{r},\Delta t), d_x(\mathbf{r}+\Delta\mathbf{r},\Delta t)\rangle$ for the x-component d_x of the measured chromatin displacements $\mathbf{d}_{ch}(\mathbf{r},\Delta t)$, where $\mathbf{r}$ is the displacement vector's position. Figure 2e shows the radially averaged $\langle C_{d_x}(\Delta r,\Delta t)\rangle$ for different Δt, with $\langle\rangle$ being the ensemble average over all $C_{d_x}(\Delta r,\Delta t)$ at a given Δt. We confirm that the spatial autocorrelation monotonously grows with an increasing Δt for $\Delta t = 0.25 - 15$ s (Fig. 2e and Supplementary Fig. 6d). Further, we assess changes in nucleus-wide chromatin dynamics before/after transcription activation by measuring the chromatin velocity amplitude $\langle|\mathbf{v}_{\mathrm{DCS}}(\Delta t)|\rangle_r = \langle|\mathbf{d}_{\mathrm{DCS}}(\mathbf{r},\Delta t)|\rangle_r/\Delta t$ averaged over the entire nucleus at each Δt (Supplementary Fig. 7). Our data show that the average nucleus-wide chromatin dynamics is unperturbed by the *MUC4* and *IL6* transcription activation stimuli, (TNFα + IFNγ) and LPS, respectively, but we do not rule out changes in the spatial distribution of chromatin velocities across the nucleus. In contrast, the average chromatin velocity in the immediate vicinity of both *MUC4* and *IL6* exhibits noticeable changes, in particular at longer timescales. Taken together, our data show no significant changes in the density of actively transcribing genes (Supplementary Fig. 5) and average nucleus-wide chromatin dynamics (Supplementary Fig. 7) upon *MUC4*/*IL6* transcriptional stimulation. This suggests that the baseline level of transcription activity in the nucleus has not changed upon these stimuli, which is in agreement with an earlier QPCR study[56].

To examine the contribution of a single gene motion (Fig. 2b) to the movement of the surrounding chromatin, and thus to the larger scale chromatin dynamics (Fig. 2c–d), we survey the concurrent movements of *MUC4* and *IL6* and their surrounding chromatin (Fig. 2f). We review these two types of motion in the gene frame, by keeping the direction of the gene displacement vector (pink and green arrows) constant and plotting the corresponding DCS field (grey arrows) of the surrounding chromatin (raw data shown in Supplementary Fig. 8a). Figure 2f presents such visualization for both inactive (pink arrow) and active (green arrow) *MUC4*/*IL6* within the context of the flows of the surrounding chromatin (grey arrows) for $\Delta t = 0.25$ and 10 s at three consecutive time steps. We find that at short timescales ($\Delta t = 0.25$ s), the motions of *MUC4* and *IL6* appear independent of the surrounding chromatin in both transcriptionally active and inactive state. Conversely, at long timescales ($\Delta t = 10$ s) active *MUC4* and *IL6* (green arrows) move in concert with the surrounding chromatin (grey arrows), but there is no visible correlation when *MUC4* and *IL6* are inactive. This suggests that the local motion of an active gene might indeed contribute to the large-scale chromatin dynamics at longer timescales.

We assess the correlation between the local gene movement and surrounding chromatin flows by computing a correlation score $S_c = \langle \mathbf{d}_g(t)/d_g(t) \cdot \mathbf{d}_{ch}(\mathbf{r},\ \Delta t)/d_{ch}(\mathbf{r},\ \Delta t)\rangle$, given by the scalar product between the displacement vectors of the gene $\mathbf{d}_g$ and of the surrounding chromatin $\mathbf{d}_{ch}$ at $\Delta t = 0.25$ s and $\Delta t = 10$ s, with $\langle\rangle$ denoting an average over all time frames. Figure 2g–h show a plot of $\langle S_c\rangle$, a radially integrated S_c averaged over a gene population, where $N(MUC4)_i = 22$, $N(IL6)_i = 17$, $N(MUC4)_a = 21$ and $N(IL6)_a = 18$ (Supplementary Table 1), as a function of the distance Δr from the gene position. Indices i and a

https://doi.org/10.1038/s41467-024-51149-4

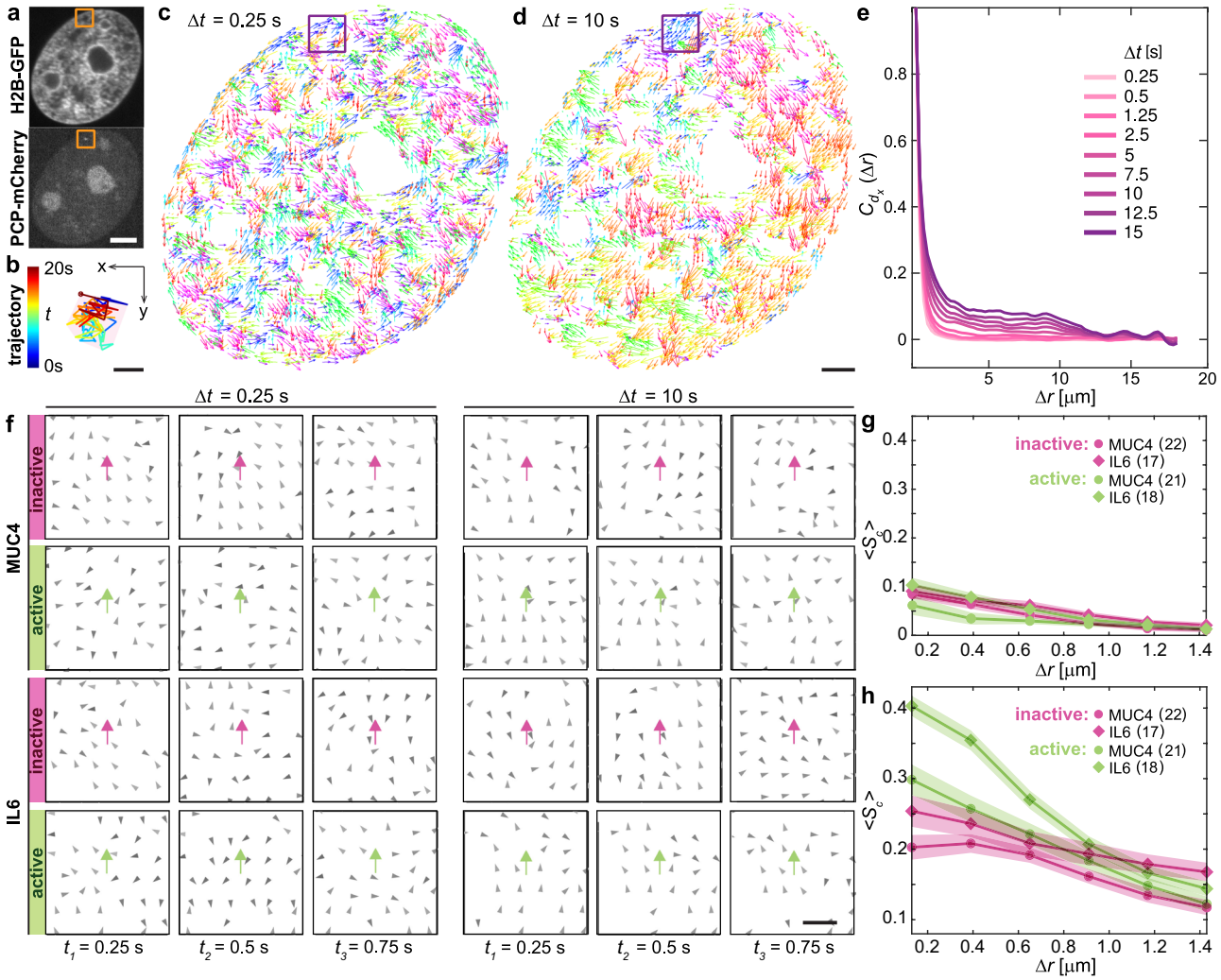

Fig. 2 | Simultaneous tracking of a gene motion and dynamics of its surrounding chromatin. a Micrographs of a nucleus with fluorescently labeled chromatin (H2B-GFP) and the *MUC4* gene locus (PCP-mCherry) (Supplementary Movies 1–2). The position of the tracked gene is marked by the orange box. **b** Trajectory of the gene from (**a**) and its area A_L over 20 s (Supplementary Movie 3). Color bar marks the time progression (from blue to red). **c** DCS maps **d**(**r**, Δt) of the nucleus computed with $\Delta t = 0.25$ s and **d** $\Delta t = 10$ s. The displacement vectors are color-coded by their direction (Supplementary Movies 4–5). The position of the tracked gene is marked by a purple box. **e** The average spatial displacement autocorrelation functions $C_{d_x}(\Delta r)$ for the nucleus from (**a**) for $\Delta t = 0.25$–15 s. **f** Chromatin displacement fields (grey arrows, DCS) around the genes of interest (pink/green arrows, SPT) at $t = 0.25$, 0.5 and 0.75 s for $\Delta t = 0.25$ s and 10 s, respectively. Magenta and green arrows correspond to gene motion in inactive and active states, respectively, detected by SPT during $\Delta t = 0.25$ and 10 s simultaneously with the DCS measurement. The DCS maps are in the gene frame, i.e., direction of gene motion is held constant (DCS maps in the nucleus frame are shown in Supplementary Fig. 8a). **g**, **h** Radially averaged correlation score $\langle S_c \rangle$ as a function of distance Δr from the gene locus, averaged over the gene population. **g** $\langle S_c \rangle$ for $\Delta t = 0.25$ s shows no visible changes upon gene activation. **h** $\langle S_c \rangle$ for $\Delta t = 10$ s increases upon gene activation at the gene locus and decreases away from it (p-values $< 10^{-3}$). Error bars show standard error. Scale bars: (**a**) 5 μm, (**b**) 100 nm, (**c**-**d**) 2 μm, (**f**) 500 nm. Source data are provided as a Source Data file.

denote inactive and active state, respectively. For $\langle S_c \rangle$ at $\Delta t = 0.25$ s, we find no correlation between motion of the genes and their surrounding chromatin, regardless of the gene's activity level (Fig. 2g). In contrast, for $\langle S_c \rangle$ at $\Delta t = 10$ s, the difference is striking: When inactive, the motion of both *MUC4* and *IL6* is not correlated with the surrounding chromatin (Fig. 2h, pink). Upon activation, however, both *MUC4* and *IL6* show about ~50% increase in their correlation with the surrounding chromatin ($\Delta r \leq 0.13\,\mu$m) at the gene center (Fig. 2h, green). The distances over which we observe high correlation are large in comparison to the diameter of chromatin fiber is ~10 nm. Remarkably, this correlation decreases 2–3 fold for active genes, but only ~20% for inactive genes over ~1.25 μm at $\Delta t = 10$ s. The decrease of correlation with the distance is expected for motion correlation caused by activity in a viscous fluid. Note, p-values of all observed changes are $\leq 10^{-3}$ (Supplementary Table 2). Thus, our results suggest that active genes might contribute to local chromatin flows.

Real-time dynamics of active and inactive genes

Next, we examine the amplitude of local displacements exhibited by a transcriptionally active versus inactive single gene and its surrounding chromatin. Figure 3a shows nuclei with CRISPR-dCas9-PCP-mCherry signal indicating the position of *MUC4*/*IL6* in the two respective states (highlighted by an orange box) and the corresponding H2B-GFP signal visualizing the surrounding chromatin. As described earlier, we track the motion of the labeled genes as well as the neighboring chromatin at temporal resolution of 250 ms over 20 s. The obtained trajectories are displayed in Fig. 3b, with time progression color-coded from blue to red. We also measure the trajectory area A_L given by the area of a convex hull (pink) enveloping the trajectory.

Further, we compute the mean square displacement for the tracked genes $MSD\ (\Delta t) = \langle |\mathbf{d}_g(t + \Delta t) - \mathbf{d}_g(t)|^2 \rangle$, with $\mathbf{d}_g(t)$ being the gene displacement at time t and average over the respective gene populations, where $N(MUC4)_i = 44$, $N(IL6)_i = 43$, $N(MUC4)_a = 42$ and

https://doi.org/10.1038/s41467-024-51149-4

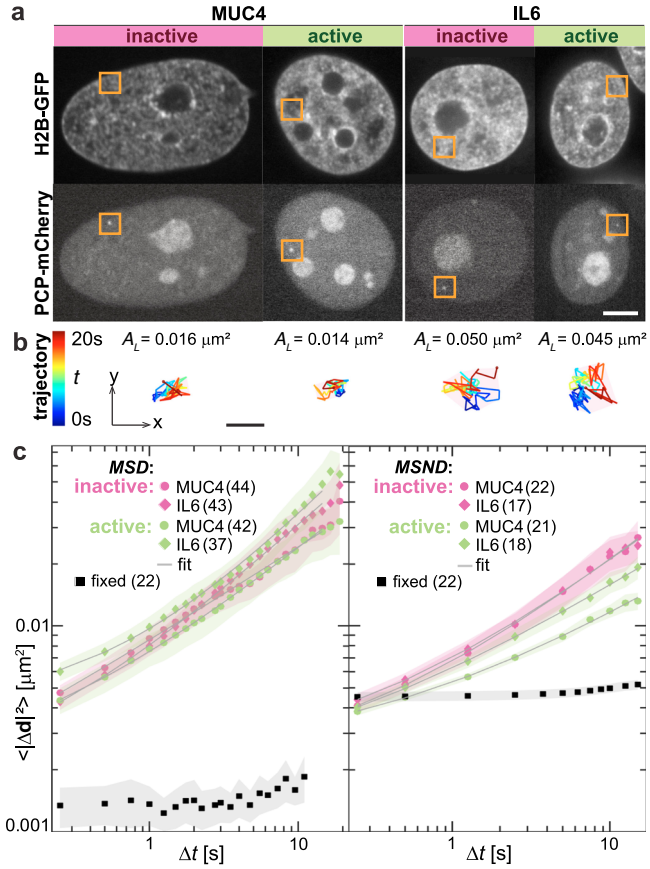

Fig. 3 | Real-time dynamics of *MUC4* and *IL6* genes in transcriptionally active/inactive states. a Micrographs of nuclei with fluorescently labeled chromatin (H2B-GFP) and *MUC4*/*IL6* (PCP-mCherry) in transcriptionally active and inactive states. The position of the gene of interest is marked by an orange box. Scale bar, 5 μm. **b** Gene trajectories from (**a**) and their areas A_L over 20 s. Color bar marks time progression (from blue to red). Scale bar, 200 nm. **c** Average $MSD(\Delta t)$ calculated for inactive *MUC4* ($N = 44$) and *IL6* ($N = 43$), active *MUC4* ($N = 42$) and *IL6* ($N = 37$). Average $MSND(\Delta t)$ calculated for chromatin motion within $\Delta r = 0.65\,\mu$m from the gene center for inactive *MUC4* ($N = 22$) and *IL6* ($N = 17$), active *MUC4* ($N = 21$) and *IL6* ($N = 18$). *N* refers to the number of genes. As a negative control, we measured *MSD* and *MSND* for *MUC4* in formaldehyde-fixed cells, showing that our measurements in vivo are well about the noise floor. The gray lines are fits to the equation $f(\Delta t) = A + B\Delta t^{\alpha}$. Error bars denote standard error. Source data are provided as a Source Data file.

$N(IL6)_a = 37$ (Fig. 3c). Surprisingly, although the *MSD* visibly changes upon activation for both genes (Fig. 3c), these changes are not statistically significant (*p*-values listed in Supplementary Table 2). However, *IL6* explores on average larger area $A_s = MSD(250\text{ ms})$ for a short timescale when active than inactive (p-value = 0.01), while *MUC4* shows no appreciable change. On the other hand, the area A_L explored over a longer time (20 s) remains similar for both genes after the activation (Supplementary Tables 3 and 4).

For the surrounding chromatin, we evaluate dynamics of chromatin in a 1.3 μm × 1.3 μm region, with the gene located in its center (Fig. 2f). We calculate the mean square network displacement[9]: $MSND\ (\Delta t) = \langle|\mathbf{d}_{ch}(\mathbf{r}, \Delta t)|^2\rangle$, where $\mathbf{d}_{ch}(\mathbf{r}, \Delta t)$ denotes the chromatin displacements at position $\mathbf{r}$. As shown in Fig. 3c, the local *MSND* reveals that for *MUC4* the surrounding chromatin is less mobile upon activation (p-value < 10^{-3}), while there is no appreciable change for *IL6* (p-value = 0.22). As a negative control, we measure *MSD* (Δt) and *MSND* (Δt) for *MUC4* in formaldehyde-fixed cells, demonstrating that both *MSD* (Δt) and *MSND* (Δt) measurements are well above the noise floor (Fig. 3c).

To evaluate the type of motion a gene undergoes at the time scale of our measurement, we fit the average *MSD* to a power law, $MSD\ (\Delta t) = A + B\Delta t^{\alpha}$. As previously shown[9,57], the constant A accounts for a possibility of an additional fast motion at time scales below our time resolution. Our data shows that for both genes A increases upon activation: for *MUC4* from $0.5 \pm 0.5 \cdot 10^{-3}\,\mu m^2$ to $1.9 \pm 0.5 \cdot 10^{-3}\mu m^2$ and for *IL6* from $1.7 \pm 0.3 \cdot 10^{-3}\mu m^2$ to $4.1 \pm 0.3 \cdot 10^{-3}\mu m^2$. We report $B = 8.0 \pm 0.5 \cdot 10^{-3}\mu m^2 s^{-\alpha}$ for inactive *MUC4* and $5.6 \pm 0.4 \cdot 10^{-3}\mu m^2 s^{-\alpha}$ for active *MUC4*, whereas $B = 6.3 \pm 0.2 \cdot 10^{-3}\mu m^2 s^{-\alpha}$ for inactive *IL6* and $5.6 \pm 0.3 \cdot 10^{-3}\mu m^2 s^{-\alpha}$ for active *IL6*. We find that both *MUC4* and *IL6* move subdiffusively ($\alpha < 1$), which is consistent with earlier studies[14,58,59]. However, our data reveals that for both *MUC4* and *IL6*, α increases upon activation from 0.47 ± 0.02 to 0.60 ± 0.02 and from 0.67 ± 0.01 to 0.7 ± 0.02, respectively (Fig. 3c & Supplementary Table 5). It is important to note that any fluorescent label may affect dynamics of its labeled structure. However, assuming similar label binding statistics for both active and inactive genes, such an effect would be comparable for genes in both states. Therefore, we interpret our results as informing on relative changes between active and inactive states, but not directly informing on the unlabeled state.

Similarly, to assess the type of motion exhibited by the chromatin surrounding the gene, we fit the average *MSND* to a power law, $MSND\ (\Delta t) = A + B\Delta t^{\alpha}$. We find that the surrounding chromatin of both genes undergoes a reduction upon activation from α ~0.6 ± 0.02 to 0.5 ± 0.02. (Supplementary Table 5). Our data suggest, that transcription activity of a gene is manifested by a dynamical signature of an increase in α for the gene motion, while the amplitude of the motion does not change appreciably. We hypothesize that genes residing in distinct local environments may be subject to different physical resistance to their motions, and hence possess a different displacement amplitude – yet, this information is lost upon averaging over all genes. Hence, to reveal the differences in displacement amplitudes between the active and inactive genes, we need to investigate motions of genes residing in a similar physical environment. In what follows, we investigate the hypothesis that the compaction of the chromatin surrounding different active genes provides varying resistance to their motion.

Chromatin compaction at active and inactive genes

To test the impact of local chromatin compaction on the mobility of a gene, we analyze the H2B-GFP signal around the gene of interest. H2B-GFP is a reliable marker of chromatin position and its relative compaction[9,57,60]. Figure 4a shows micrographs of *MUC4* and *IL6* (CRISPR-dCas9-PCP-mCherry, orange circle) in inactive/active state and the surrounding chromatin (H2B-GFP). The orange cross in the H2B-GFP signal marks the position of the gene center and the grey solid and dashed circles denote the 0.5 μm and 1 μm distances from the gene center, respectively. The difference in the compaction of chromatin surrounding different genes is clearly visible as variations in the H2B-GFP intensity.

To quantify differences in the chromatin compaction, we evaluate I_{ch}, the H2B-GFP intensity I measured at the gene center at $t = 0$ s and normalized by the average H2B-GFP intensity in the entire nucleus $\langle I \rangle$. $I_{ch} = I(0)$ is representative of the chromatin compaction over the 20 s observation time in our experiments (Supplementary Fig. 9). Figure 4b shows distributions of I_{ch} obtained for populations of inactive and active *MUC4* and *IL6* genes. While the mean I_{ch} value does not change significantly upon activation of *MUC4* or *IL6*, a closer inspection of the distributions reveals a presence of two distinct modes in all 4 populations: one at $I_{ch} < 1$, another at $I_{ch} > 1$. Since $I_{ch} = 1$ corresponds to the average H2B-GFP intensity in the nucleus (Fig. 4b, grey line), $I_{ch} < 1$ corresponds to a lower and $I_{ch} > 1$ to higher chromatin compaction. This suggests that for both inactive and active *MUC4*/*IL6* we find genes that are located in less as well as more compact chromatin, indicating that each gene might have a rather unique local environment. The

https://doi.org/10.1038/s41467-024-51149-4

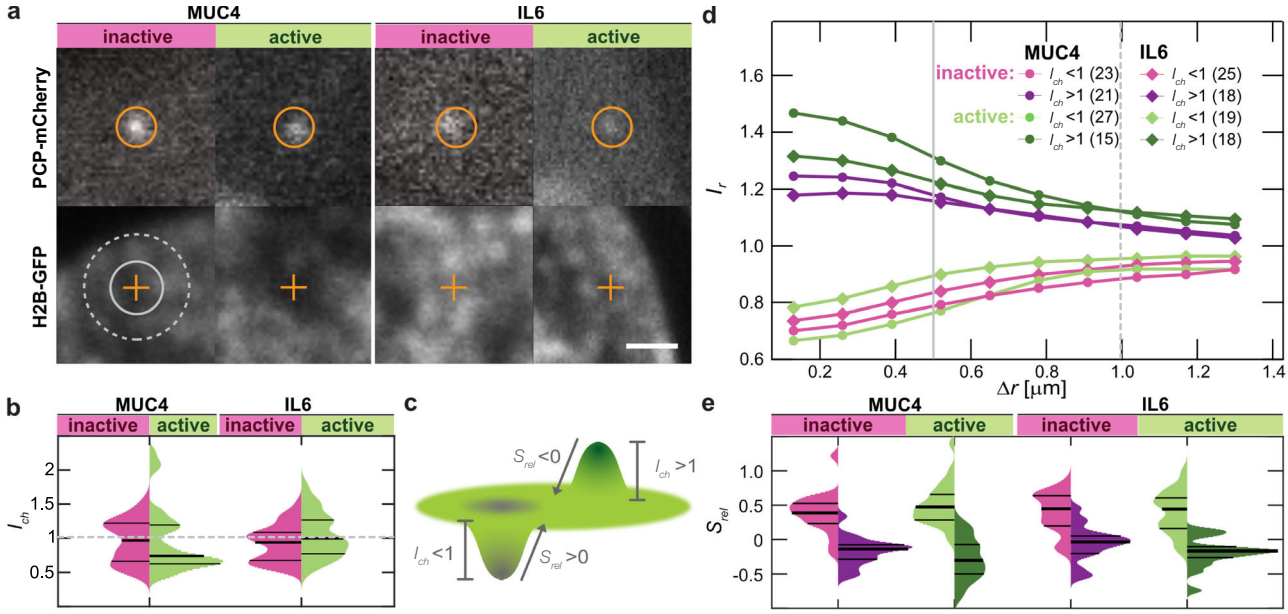

Fig. 4 | Chromatin compaction as a function of gene's transcriptional activity. **a** Micrographs of *MUC4* and *IL6* genes (PCP-mCherry) in transcriptionally inactive and active states (highlighted by orange circles) and their surrounding chromatin (H2B-GFP) with the gene locus center marked by an orange cross. Grey circles denote 0.5 μm (solid line) and 1 μm (dashed line) distance from the gene center. **b** Distribution of I_{ch}, H2B-GFP intensity at a gene center normalized by the average H2B-GFP intensity in the nucleus, for inactive *MUC4* ($N = 44$) and *IL6* ($N = 43$), active *MUC4* ($N = 42$) and *IL6* ($N = 37$). **c** Schematics of parameters describing chromatin compaction states: low compaction, $I_{ch} < 1$ and $S_{rel} > 0$, and high compaction, $I_{ch} > 1$ and $S_{rel} < 0$. **d** $I_r(\Delta r)$ for *MUC4* and *IL6* localized in chromatin of low compaction ($I_{ch} < 1$, pink and light green) and high compaction ($I_{ch} > 1$, magenta and dark green). **e** Distributions of S_{rel}, relative change of the H2B-GFP intensity over distance Δr from the gene center, for *MUC4* and *IL6* in inactive (magenta) and active (green) states, further sorted by the local chromatin compaction (I_{ch}) introduced in (**d**). In (**b**) and (**e**), the black lines correspond to 25%, 50% and 75% quartiles. Scale bar, 1 μm. Source data are provided as a Source Data file.

schematics in Fig. 4c illustrates these different chromatin compaction states by depicting the local H2B-GFP intensity (green). In addition to I_{ch}, it introduces S_{rel}, which assesses the H2B-GFP intensity change over 0.75 μm from gene by measuring its linear slope[57]. The means and standard errors for measured I_{ch} and S_{rel} are listed in Supplementary Table 3.

Next, we measure $I_r(\Delta r)$, the chromatin compaction as a function of the distance Δr from the gene, by radially averaging H2B-GFP intensity over 0.13 μm increments and normalizing by $\langle I \rangle$ (see *Methods*). Note, the first point of $I_r(\Delta r)$ corresponds to I_{ch}. We sort both inactive and active genes by their local chromatin compaction I_{ch}, specifically, low compaction ($I_{ch} < 1$) and high compaction ($I_{ch} > 1$) chromatin, and obtain average $I_r(\Delta r)$ for both genes in each chromatin compaction state (Fig. 4d). Strikingly, our data reveal that both active genes can be found in both less and more compact chromatin, similarly, both inactive genes do not show a strict preference for a specific compaction state. We further confirm this finding by measuring I_{ch} at *IL6* and *MUC4* nascent RNA sites visualized by RNA FISH (Supplementary Fig. 3) and finding that active loci can indeed exist with similar probability in both low and high chromatin compaction states.

To further explore a possible correlation between the local chromatin compaction and the activity of genes, we have performed the same analysis for all active transcription sites in a cell, providing us with much larger statistics. Specifically, we used IF labeling of active RNA pol II (N = 1661 over 50 cells) and evaluated the chromatin compaction in their vicinity (Supplementary Fig. 10e). We find that ~80% of active transcription sites are located in less compact chromatin ($I_{ch} < 1$) and ~20% in more compact chromatin ($I_{ch} > 1$) (Supplementary Fig. 10f). This observation is consistent with previous studies, which found transcription to occur predominantly (but not exclusively) in less compact chromatin[32,36–38,61]. Moreover, our data show that average chromatin compaction at active RNA poll II sites is intermediate with $\langle I_{ch} \rangle \sim 0.9$, which is in agreement with an earlier study[61]. When we evaluate S_{rel} for all the states introduced in Fig. 4d, we find that independently of their activity, genes located in $I_{ch} < 1$, show higher S_{rel} values, while genes located in $I_{ch} > 1$, have lower S_{rel} values (Fig. 4e, Supplementary Table 3). Therefore, while many active genes tend to locate in less compact chromatin, it is critical to survey the unique properties of the local environment of each active gene in order to elucidate the physical mechanism underlying their dynamics.

Contribution of active genes to coherent chromatin motions

To further examine the impact of local chromatin compaction on the mobility of inactive and active genes, we sort genes by their local chromatin compaction I_{ch} and compute the corresponding *MSD* and *MSND*. We then evaluate the time dependence of *MSD* and *MSND* by fitting it to $f(\Delta t) = A + B\Delta t^{\alpha}$. As shown in Fig. 5a, we find that *MSD* of single genes strongly depends on both their chromatin compaction I_{ch} and their transcriptional state. Specifically, inactive *MUC4* and *IL6* have surprisingly similar behavior, with their *MSD* showing significantly larger displacements and α (and thus higher mobility), for genes located in less compact chromatin ($I_{ch} < 1$, Fig. 5a, pink curves) than in more compact chromatin ($I_{ch} > 1$, Fig. 5a, magenta curves), with p-values $< 10^{-3}$ (Supplementary Table 2). Upon activation, *MUC4* and *IL6* located in more compact chromatin show no significant changes in their mobility ($I_{ch} > 1$, Fig. 5a, dark green curves) compared to their inactive state. However, active *MUC4* and *IL6* located in less compact chromatin exhibit remarkably different behavior ($I_{ch} < 1$, Fig. 5a, light green curves) from their inactive counterparts. While α increases for both *MUC4* and *IL6* genes located in less compact chromatin upon activation ($I_{ch} < 1$, Fig. 5a, light green curves), the absolute values of their displacements do not appreciably change for *IL6*, but decrease significantly for *MUC4* (p-value = 0.01), when compared to their *MSD* in inactive state. This suggests that the genes located in more compact chromatin are more constrained by the surrounding chromatin and thus the effect of their activity on their mobility is weak. Conversely, genes whose surrounding chromatin has a lower compaction can move easily,

https://doi.org/10.1038/s41467-024-51149-4

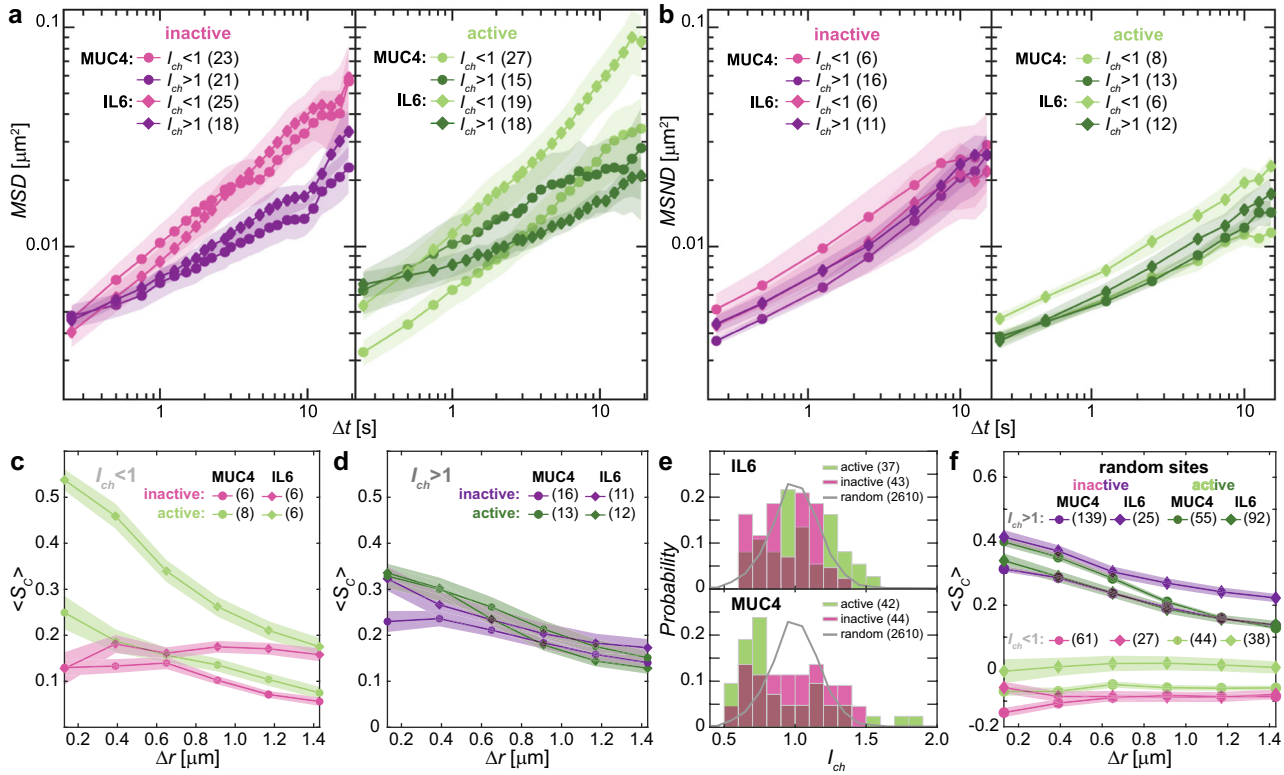

Fig. 5 | Active genes drive chromatin coherent motion. a The average *MSD* measured for *MUC4*/*IL6* gene loci in both inactive (magenta) and active (green) states, and sorted by the local chromatin compaction I_{ch}. **b** The average *MSND* measured for chromatin surrounding the *MUC4*/*IL6* gene loci in both inactive (magenta) and active (green) states, and sorted by local chromatin compaction I_{ch}. **c** Average correlation score $\langle S_c \rangle$ as a function of distance Δr from the gene for *MUC4*/*IL6* located in low compaction chromatin ($I_{ch} < 1$), in both inactive and active states. **d** Average $\langle S_c \rangle$ as a function of distance from the gene for *MUC4*/*IL6* located in high compaction chromatin ($I_{ch} > 1$), in both inactive and active states. **e** I_{ch} distributions at *IL6* sites (top) and *MUC4* sites (bottom) in transcriptionally inactive/active states, and at random sites (gray line). **f** $\langle S_c \rangle$ computed for random sites with similar chromatin compaction profiles as *IL6* and *MUC4* sites in the nucleus, and sorted by compaction in the same way as data in (**c**) and (**d**). Error bars denote standard error. Source data are provided as a Source Data file.

allowing us to investigate their contribution to the local chromatin dynamics.

In contrast, Fig. 5b displays the *MSND* of the chromatin surrounding the genes: For *MUC4* upon transcriptional activation, its *MSND* decreases significantly in both compaction states (p-values ≤ 0.04). Whereas, for *IL6* upon transcriptional activation, we observe significant decrease in *MSND* only at higher chromatin compaction ($I_{ch} > 1$, p-value = 0.03). Moreover, when we assess the amplitude of the average velocity $\langle |\mathbf{v}_{DCS}(\Delta t)| \rangle$ of the chromatin surrounding the gene, we find a decrease for chromatin surrounding the active genes (Supplementary Fig. 7), which is consistent with the above observations. The fitting parameters and their errors from both *MSD* and *MSND* are shown in Supplementary Table 5 and the p-values in Supplementary Table 2.

Our observations suggest that the dynamic behavior of genes upon their transcriptional activation largely depends on the compaction of their surrounding chromatin (Fig. 5a). We confirm this by computing the average correlation score $\langle S_c \rangle$ at $\Delta t = 10$ s for groups of genes located in chromatin of the same compaction I_{ch} (Fig. 5c–d). Indeed, we find that genes residing in lower compaction chromatin exhibit dramatic difference in $\langle S_c \rangle$ upon activation, especially *IL6* showing an increase from ~0.1 to ~0.5 at $\Delta r \leq 0.13\,\mu$m (Fig. 5c). For both *MUC4* and *IL6* in low compaction chromatin, the $\langle S_c \rangle$ significantly increases upon activation (p-values < 10^{-3}). Interestingly, $\langle S_c \rangle$ decreases with increasing distance from the gene until reaching the values comparable to inactive genes at ~1.4 μm, thus leading to regions of coherent motion of ~2.8 μm. This is in excellent agreement with the size of coherent regions (~3–5 μm) measured by DCS[9]. Inactive genes do not show any changes in $\langle S_c \rangle$ with increasing distance from the gene. In contrary, genes residing in more compact chromatin show a slight correlation (~0.3) in both active and inactive states (Fig. 5d, Supplementary Table 1). This suggests an orientational order of local chromatin motions, which likely arises due to tight physical coupling within regions of high chromatin compaction. Hence, larger regions of chromatin move together, when they are in more condensed state (e.g., heterochromatin).

To validate our observation of gene mobility depending on both its local chromatin compaction and transcriptional state, we assess the mobility and chromatin compaction of random genomic sites as a control measurement. Naturally, random sites will vary in their physical properties (size/compaction/intensity distribution). To enable comparison of motions of random sites and *MUC4*/*IL6* gene loci, we choose only a subset of random sites that have physical properties identical to those of *MUC4*/*IL6* active (or inactive) sites. We identify such random sites as mock active (or inactive) sites and track their motions. Specifically, using a previously published machine-learning algorithm[57], we first generate a population of random sites across the entire nucleus in the H2B-GFP signal, for which we measure I_{ch} and S_{rel}. Hence, we next identify subpopulations of these random sites whose I_{ch} and S_{rel} match those of the H2B-GFP signal at *MUC4*/*IL6* genes in inactive/active states (Fig. 5e). This yields eight distinct random sites groups that match I_{ch} and S_{rel} of *MUC4*/*IL6* in the different studied states: inactive/active *MUC4*/*IL6* in low/high compaction chromatin. Once these groups of random sites are established, we track the motion of each random site over the same time interval (20 s) as we did for *MUC4*/*IL6* and calculate their average correlation score $\langle S_c \rangle$ at $\Delta t = 10$ s with the surrounding DCS fields (Fig. 5f, Supplementary Table 1). Our data reveal that the motion of random sites in more

https://doi.org/10.1038/s41467-024-51149-4

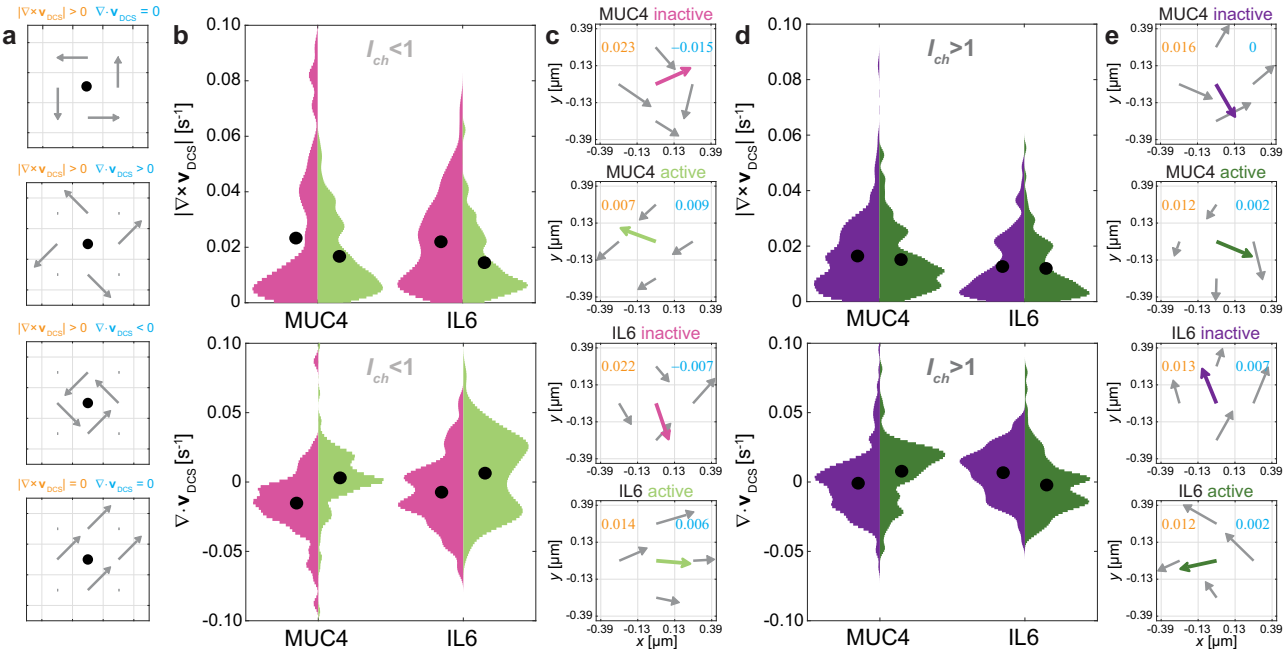

Fig. 6 | Vorticity and divergence of chromatin velocity fields surrounding *MUC4* and *IL6* genes. a Vorticity $|\nabla \times \mathbf{v}_{DCS}|$ (orange) and divergence $\nabla \cdot \mathbf{v}_{DCS}$ (blue) of canonical cases. **b** Vorticity and divergence of the velocity field $\mathbf{v}_{DCS}(\mathbf{r}, \Delta t)$ for $\Delta t = 10$ s at gene sites with low chromatin compaction ($l_{ch} < 1$). Pink and green denote inactive and active cases, respectively. **c** Representative fields from (**b**), where orange and blue colored values denote the vorticity and divergence measurement, respectively. Pink and green arrows mark motion of inactive and active genes, respectively. **d** Vorticity and divergence of the velocity field $\mathbf{v}_{DCS}(\mathbf{r}, \Delta t)$ for $\Delta t = 10$ s at gene sites with high chromatin compaction ($l_{ch} > 1$). Purple and dark green denote inactive and active cases, respectively. **e** Representative fields from (**d**), where orange and blue colored values denote the vorticity and divergence measurement, respectively. Purple and dark green arrows mark motion of inactive and active genes, respectively. The black dot denotes the average value of the distribution. Source data are provided as a Source Data file.

compact chromatin shows indeed an inherent correlation with the surrounding chromatin, whereas random sites in less compact chromatin show on average no correlation (Fig. 5f). This suggests that local chromatin compaction affects the mobility of gene loci. Moreover, it is consistent with a picture of active genes driving the coherent motions in low compaction chromatin.

Gene activity and chromatin compaction affect chromatin flow alignment

To assess the effect of transcriptional activity of a single gene on the surrounding chromatin flow, we analyze these flows before/after the gene's activation. To this end, we measure the divergence and vorticity (curl) of chromatin velocity fields directly around the gene site. Roughly speaking, the divergence of a velocity field measures the tendency of the surrounding chromatin fluid to collect or disperse at the gene site, whereas the curl of a velocity field measures the tendency of the chromatin fluid to circulate around the gene. We obtain the velocity fields from the DCS-measured displacement fields as $\mathbf{v}_{DCS}(\mathbf{r}, \Delta t) = \mathbf{d}(\mathbf{r}, \Delta t)/\Delta t$.

We specifically choose to measure the divergence and curl over the timescale $\Delta t = 10$ s, where the large-scale coherent chromatin motions occur, while at shorter timescales (<1 s) local chromatin displacements are uncorrelated[9]. Both, the fast uncorrelated motion and slow coherent motion happen concurrently. However, the large-scale coherency was shown to be eliminated upon ATP depletion as well as RNA pol II inhibition[9,23,24], suggesting that active processes drive large-scale coherency. Importantly, the chromatin coherency in vivo has a lifetime of 5–10 s, after which the coherent regions break-up, new ones form and move into new directions[9]. Thus, to examine the effect of active transcriptional events on the coherent motions, it is informative to analyze the vector field characteristics over 10 s.

Figure 6 a illustrates four canonical cases, where a 2D velocity field would exhibit some circulation ($|\nabla \times \mathbf{v}_{DCS}| > 0$) or no circulation ($|\nabla \times \mathbf{v}_{DCS}| = 0$), while also exhibiting net flow inward ($\nabla \cdot \mathbf{v}_{DCS} < 0$), net flow outward ($\nabla \cdot \mathbf{v}_{DCS} > 0$), or equal inward and outward flow ($\nabla \cdot \mathbf{v}_{DCS} = 0$). Unlike the direction of flow in or out of a region, the direction of the circulation is not relevant. In order to read out vorticity and divergence at a gene site, the nearest four displacement vectors of DCS calculated at $\Delta t = 10$ s are evaluated. We find that upon transcriptional activation, the magnitude of the vorticity is significantly reduced (p-values ≤ 0.01) for both genes when located in low compaction chromatin (Fig. 6b, top, and Supplementary Table 6), while remaining the same for both genes when located in high compaction chromatin (Fig. 6d, top, and Supplementary Table 6). Notably, upon activation we observe for both genes a significant increase in the divergence values from negative (inwards flows) to positive (outward flows), with the divergence distributions showing a strong shift upward (p-values < 10^{-3}), when located in low compaction chromatin (Fig. 6b, bottom, and Supplementary Table 6). Interestingly, *IL6* divergence exhibits a bimodal distribution, while *MUC4* divergence exhibits a trimodal distribution with a dominant peak at $\nabla \cdot \mathbf{v}_{DCS} \sim 0$. In contrast, upon activation of genes in high compaction chromatin, we observe opposite trends for divergence distributions of the two genes: While for *MUC4* the distribution shifts to higher values, for *IL6* it moves to lower values (Fig. 6d, bottom, and Supplementary Table 6). A non-zero divergence indicates chromatin acts as a compressible material, which is consistent with the fact that chromatin can condense and decondense within its solvent. Given the 5–10 s lifetime of chromatin coherency, it is unlikely that any given active site exhibits single-signed divergence over long times. This is consistent with wide distributions in Fig. 6b and d, spanning both negative and positive values.

Close inspection of individual chromatin displacement fields reveals that upon transcriptional activation chromatin flows align with the motion of the active genes in low compaction chromatin (Fig. 6c, gray arrows). This is in contrast to inactive genes in low compaction chromatin, whose surrounding chromatin flows are not aligned. We

find that for active genes local chromatin flows display higher alignment, when $|\nabla \times \mathbf{v}_{DCS}| < 0.02\,s^{-1}$, as higher vorticity introduces visible misalignment of the flows. This suggests that at low compaction chromatin, active genes may be involved in the alignment of the surrounding chromatin flows.

In contrast, we find for both genes when they are located in high chromatin compaction, that the surrounding chromatin flow is aligned before and misaligned after activation (Fig. 6e, gray arrows). This corroborates our findings in Fig. 5f suggesting that high compaction chromatin induces an inherent correlation due to a tight physical coupling of the chromatin polymeric network (e.g., heterochromatin). Polymer entanglements can serve as topological crosslinks and thus effectively cause an elastic coupling of the neighboring chromatin fibers. Taken together, these results suggest that active transcription sites may be contributing to the coherent chromatin motions.

Discussion

In this work, we developed an approach, which allows to simultaneously monitor motion of a single gene and its surrounding chromatin, while controlling the gene's transcriptional activity in vivo. It employs a combined platform of CRISPR-dCas9-PCP-mCherry system, simultaneous two-color spinning disc microscopy, single particle tracking and displacement correlation spectroscopy (DCS). Our approach reveals dynamical signatures of transcriptionally active genes and their contribution to the motion of the surrounding chromatin, providing insight into large-scale chromatin motions in the cell nucleus. In particular, we investigate the contribution of active genes to the micron-scale coherent chromatin motion.

Notably, we find that if we evaluate a motion of single genes before and after transcriptional activation averaged over a gene population, the average gene motion of both active and inactive gene populations is quite similar. However, if we sort the active/inactive genes by their local chromatin compaction (high vs. low), the motions of active vs. inactive genes located in the chromatin of the same compaction are strikingly different, with distinct dynamical signatures. This suggests that the physical properties of the immediate environment of the gene play a key role in the gene's mobility. Moreover, these results reveal that the same gene can reside in different chromatin compaction levels upon transcriptional activation. Below, we discuss these results in greater detail and provide possible interpretations.

Specifically, our results suggest that mobility of a gene in both active and inactive states is modulated by the compaction of the surrounding genome. The local chromatin compaction was shown to be directly linked to its material properties, with low compaction chromatin being largely viscous (easy to deform), and high compaction chromatin being predominantly elastic (hard to deform)[39]. Therefore, different compaction (and thus material properties) of each gene's local environment, would provide a varying level of resistance to the forces from the active transcription machinery[39,62]: Higher chromatin compaction indicates denser chromatin packing and thus larger resistance to the gene's motion, while a lower compaction implies less dense chromatin packing, i.e., lower resistance. Indeed, we find that genes located in less compact chromatin are much more mobile than those in more compact chromatin, regardless of their activity state. Thus, an inactive gene in low compaction chromatin might be more mobile than an active gene in high compaction. Taken together, the mobility of a gene seems to depend on both its transcriptional state as well as its local chromatin compaction. This fundamental insight might aid in unifying results from earlier studies, which reported genes of reduced as well as enhanced movement upon their activation[16,32–35].

To further explore the link between dynamics of a single gene and its environment, we have investigated the concurrent motion, i.e. flows, of the surrounding chromatin. As mentioned above, we uncovered that active genes can reside in both higher as well as lower compaction chromatin. The surrounding chromatin of lower compaction shows on average higher mobility than its higher compaction counterpart. However, the absolute values of displacements experienced by active genes appear to be gene-specific. This difference may stem from the different sizes of *MUC4* and *IL6* genes. As recently suggested, large genes densely decorated with RNA pol II can become stiffer, forming loops with an increased persistence length[63]. Hence, it is possible that the persistence length of *MUC4*, which is a long gene, may increase upon activation. This would in turn lead to an effective increase in its hydrodynamic radius, making it less mobile in its active than its inactive state. Conversely, this effect would be less appreciable upon activation of smaller genes such as *IL6*, and the gene's hydrodynamic radius would remain small, making small active genes effectively more mobile than large active genes in the environment of similar chromatin compaction. This picture is consistent with the fact, that motion of a smaller gene *IL6* is strongly aligned with the surrounding chromatin flow field, while motion of a larger gene *MUC4* is less aligned. In addition, local nucleopasmic flows generated by the transcriptional activity may also contribute to difference in dynamical signatures of small and large active genes, by affecting the local conformation of the chromatin fiber[64,65].

Importantly, the neighboring chromatin might contain both active and inactive genes contributing to its observed dynamics and thus present an active system itself[64]. To assess the contribution of a single active gene to the dynamics of the surrounding chromatin, we survey the directions of these concurrent motions. Strikingly, we find that the coupling between single gene and surrounding chromatin motions is closely linked to the local chromatin compaction. Motion of a gene located in more compact chromatin shows a weak non-zero correlation (~0.3) with the surrounding chromatin independent of gene's activity. This correlation may be explained by tight chromatin packing, leading to more topological crosslinks, and thus physically linking motion of neighboring chromatin segments. We can interpret this situation as an elastic coupling. This hypothesis was corroborated by reviewing behavior of random chromatin sites, where random sites located in more compact chromatin showed the same inherent correlation of ~0.3, while random sites residing in less compact chromatin show no correlation. This suggests that by observing motion of genes in less compact chromatin, we may be able to learn about their unbiased contribution to the coherent chromatin motion. Indeed, the difference between the dynamical behavior of active and inactive genes is striking. While inactive genes show no significant correlation (~0.1) with the motion of the surrounding chromatin, active genes are highly correlated (~0.5).

Recently, a physical picture emerged from models that investigate the effect of active forces on chromatin dynamics in the presence of the nucleoplasm[23,24,64–68]. In this framework, nucleoplasm-mediated hydrodynamic coupling between active forces applied on chromatin fiber can induce large-scale coherency in chromatin motions. In addition, active forces were represented in form of a force dipole[23,24], which consists of two equally large, but opposite forces, corresponding to a force that a nuclear ATPase exerts on the chromatin fiber and an opposite force applied on the surrounding nucleoplasm by virtue of Newton's third law. This raises question whether we can reconcile our newly reported results with such a physical framework. One possible interpretation of our observations is that active forces applied on the chromatin fiber during a transcriptional event may induce coherence in motion of the surrounding chromatin. Such active forces could originate from RNA pol II but also from other transcription-related machinery that binds to the chromatin fiber and exerts forces, e.g. chromatin remodelers[55]. Indeed, high correlation between motions of active genes and the surrounding low compaction chromatin could be explained by the nucleoplasm-mediated hydrodynamic coupling of active forces acting on the chromatin fiber[23,24,64–76].

Considering our observations and the physical framework described above, we propose a following biophysical mechanism

https://doi.org/10.1038/s41467-024-51149-4

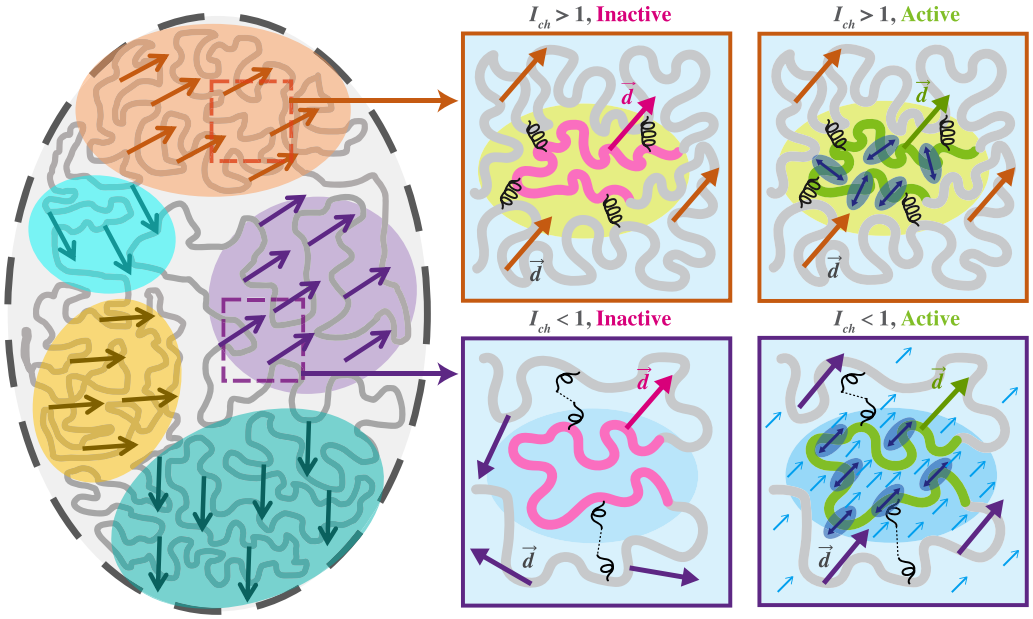

Fig. 7 | Cartoon of a proposed biophysical mechanism behind coherent chromatin motions. Regions of coherent chromatin motions are depicted by different colors with arrows indicating chromatin displacements within those regions. Insets illustrate different proposed effects of active forces rooted in a gene's transcriptional activity on its immediate environment, depending on the compaction of the gene's surrounding chromatin: (Top, orange insets) A gene located in high compaction chromatin ($I_{ch} > 1$) may be tightly coupled to its dense chromatin environment by elastic entanglements (illustrated by black springs), and thus motion of both inactive (pink) and active (green) genes would be correlated with that of the surrounding high compaction chromatin. Active forces originating from gene's transcriptional activity are illustrated as force dipoles (blue double arrows) acting on the chromatin fiber of the active (green) gene. (Bottom, purple insets) A gene located in low compaction chromatin ($I_{ch} < 1$) may be only loosely coupled to its surrounding chromatin (illustrated by black dotted springs), so motion of inactive genes (pink) would then not be correlated with motions of their surrounding chromatin. In contrast, active (green) genes are subject to active forces (illustrated as force dipoles, blue double arrows), which might affect both the chromatin fiber as well as the surrounding fluid. Hydrodynamic coupling may then align the force dipoles, giving rise to coherent chromatin motions (purple arrows) and local nucleoplasmic flows (small light blue arrows) as predicted earlier[23,24]. This model presents one possible interpretation of our findings.

connecting transcription-dependent motions of single genes with motions of their surrounding chromatin (Fig. 7): We propose that the contribution of active forces rooted in the gene's transcription activity to the motion of the surrounding chromatin is closely linked to the chromatin compaction at and around the gene site. Specifically, if a gene is located in a region of high chromatin compaction ($I_{ch} > 1$, Fig. 7, orange insets), it may be elastically coupled to its immediate environment by polymeric entanglements or topological crosslinks (black springs). In such case, the gene's motion would be dominated by the coherent chromatin motions of the surrounding region (parallel orange arrows within orange insets), independently of the gene's activity. The active forces rooted in transcriptional activity are illustrated as force dipoles (blue double arrows) acting on the gene. In contrast, if a gene is located in a region of low chromatin compaction ($I_{ch} < 1$, Fig. 7, purple insets), its coupling to the immediate environment may be weak (black dotted springs). In this case, motion of an active gene would be dominated by the active forces acting on it (blue double arrows). These active forces may then interact hydrodynamically, leading to their alignment and thus generating coherent chromatin motions at and around the active gene. This is but one possible interpretation of our findings.

Of course, active forces rooted in transcription might be only one of many possible dipolar activities, which could be leading to coherent chromatin motions in the nucleus. Other active processes such as replication, may also locally contribute active forces needed for chromatin coherency. However, given that transcriptional events occur throughout the interphase, in contrast to processes such as replication, which occurs only in certain stages of the cell cycle, we speculate that transcription-rooted active forces may be the dominant contributor to the coherent chromatin motion.

In conclusion, our study presents an experimental and analytical platform to investigate dynamical properties of single genes within the larger context of their physical environment. Our findings suggest that transcriptionally active sites contribute to the coherent chromatin motions, with active genes having a characteristic dynamical signature, strongly susceptible to the physical properties of their surroundings. Such knowledge provides insights into the biophysical mechanisms behind coherent chromatin motion, which leads to a collective motion of genes over several seconds. This might have implications for the spatiotemporal evolution of gene regulation, directly impacting the timescales and length scales of genomic interactions. Furthermore, our findings might help to understand the 4D dynamic self-organization of the human genome in the cell nucleus. Finally, our experimental and data-analytical platform can be applied to many other systems, such as different cell lines or cell states, enabling future studies of the genome dynamics in health and disease.

Methods

Cell culture

The stable HeLa H2B-GFP cell line was a gift from Tim Mitchison, Harvard Medical School, Boston, and was cultured according to the American Type Culture Collection recommendations. To generate a stable HeLa H2B-GFP dCas9-Puro cell line, HeLa H2B-GFP cells were transfected with the retroviral plasmid MSCVLTR-dCas9-puro[42] using Lipofectamine 2000 (Invitrogen) following the manufacturer's protocol, and followed by a puromycin (Sigma Aldrich) selection. MSCVLTR-dCas9-puro plasmid was a kind gift from Jane Skok, New York University School of Medicine. Cells were cultured in a humidified, 5% CO_2 (vol/vol) atmosphere at 37 °C in Gibco Dulbecco's modified eagle medium (DMEM) supplemented with 10% FBS (vol/vol), 100 units/mL penicillin, 100 μg/mL streptomycin (Invitrogen), 5 μg/mL Plasmocin

Prophylactic (Invivogen) and 0.7 μg/mL puromycin. For fluorescence in situ hybridization (FISH) (see *Methods*) and fixation experiments, cells were fixed with 3.7% formaldehyde in phosphate-buffered saline (PBS) at room temperature for 20 min and then washed three times with PBS every 5 min. Coverslips were mounted on the glass microscope slides using Prolong-Diamond Antifade Reagent (Invitrogen).

Delivery of dCas9, PP7-coat proteins and sgRNAs

For transfection experiments, 2.5 x 10^4 of stable HeLa H2B-GFP dCas9-puro cells were plated on Nunc™ Lab-Tek™ II 8-well chambered cover glass No.1.5 (Thermo Scientific) and transfected 24 hr later. The cells were transiently transfected with a mixture of 150 ng MSCVLTR-dCas9-puro plasmid, 50 ng PCP-mCherry[42] and 800 ng sgRNA(s) (sgTelomere-PP7, sgMUC4-PP7 or cocktail of 67 sgIL6-PP7, respectively) using Lipofectamine 2000 (Invitrogen) following the manufacturer's protocol. The MSCVLTR-dCas9-puro, lenti-mU6-LacZ-PP7-1 and PCP-mCherry plasmids were a kind gift from Jane Skok, New York University School of Medicine. The sgRNA sequences are listed in Supplementary Table 7. 48 hr after transfection, cell medium was replaced by Gibco CO_2-independent medium supplemented with L-glutamine (Invitrogen). The sample was then mounted on the microscope stage kept in a custom-built 37 °C microscope incubator enclosure with 5% CO_2 (vol/vol) delivery during the entire experiment. The positions of imaged cells were recorded and saved. To measure the absolute yield of gene labeling, all focal planes of each nucleus need to be scanned, which, however, affects the signal quality of image streams subsequently collected for gene motion tracking. To avoid that, we immediately focused on tracking a gene within a single plane. In this way, we found single genes labeled in 20% of nuclei, which is a lower bound estimate, given our procedure. Signal-to-noise ratio of the PCP-mCherry-labeled gene loci is shown in Supplementary Fig. 2a.

Transcriptional activation of *MUC4* and *IL6*

For transcriptional activation of *MUC4*, cells were incubated with 200 IU/mL IFNγ and 25 ng/mL TNFα for 20 hr before imaging. For transcriptional activation of *IL6*, cells were incubated with 1 μg/mL Lipopolysaccharide (LPS) for 30 min before imaging. Transcriptional activation of *MUC4* and *IL6* was confirmed by RNA FISH staining of nascent *MUC4* and *IL6* RNA as well as by immunofluorescent labeling of active RNA pol II (Ser5) (see *Methods*).

DNA constructs

The MSCVLTR-dCas9-puro, lenti-mU6-LacZ-PP7-1 and PCP-mCherry plasmids were a kind gift from Jane Skok, New York University School of Medicine. Lentiviral murine-U6-driven sgRNA-PP7-1 plasmids containing target sequences were generated by replacing LacZ in the lenti-mU6-LacZ-PP7-1 plasmid with a PCR-amplified fragment of sgRNA-PP7. To generate insertions containing the target sequence, a forward primer 5′-TTGGAGAACCACCTTGTTGGN_{17-21}GTTTTAGAGCTA-3′, was used, where N_{17-21} is the target sequence with the size of 17–21 bp. Each forward primer was mixed with an equal amount of the reverse primer, then new sgRNA fragments were obtained by PCR amplification using lenti-mU6-LacZ-PP7-1 plasmid as the template. For telomeres and *MUC4*, target sequences previously published in ref. 14 were used. For *IL6*, 67 non-repetitive target sequences were identified using Benchling[77]. The PCR reaction was performed using the Phusion Master Mix (Thermo Scientific) under the following conditions: 98 °C for 30 s; 98 °C for 20 s, 62 °C for 20 s, 72 °C for 10 s and repeated 35 times; 72 °C for 5 min; 4 °C hold. After the PCR, the products were separated on a 1% agarose gel and purified by extracting the ~200 bp DNA band. sgRNA-PP7 were constructed by fusing the purified DNA and linearized lenti-mU6 vector by the following PCR reaction (forward primer: 5′-TTTGAATTCGTCGAGGGACCTA-3′, reverse primer: 5′-CCAACAagg TGGttctccaa-3′) using Gibson assembly. sgMUC4-PP7 was also made by ligating purified sgMUC4 and lenti-mU6-Lacz-PP7 digested by BstXI and EcoRI using T4 DNA ligase (NEB). sgMUC4-PP7 prepared by both methods were validated by sequencing (GeneWiz). The sequence used for the sgRNA-PP7-1 scaffold was: 5′-N_{17-21}GUUUUAGAGCUAUAA GGAGUUUAUAUGGAAACCCUUAUAGCAAGUUAAAAUAAGGCAGUCC GUUAUCAACUUGGCCUAAGGAGUUUAUAUGGAAACCCUUAGGCCAA GUGGCACCGAGUCGGUGCUUUUUUU-3′. The target sequences of the 67 sgRNAs for *IL6* are listed in Supplementary Table 7.

Fluorescence in Situ Hybridization (FISH)

After H2B-GFP and CRISPR-dCas9-PCP-mCherry signals were imaged in live cells, the cells were fixed with 3.7% formaldehyde in PBS at room temperature for 20 min and then washed three times with PBS every 5 min. For telomeres, cells were consecutively dehydrated in 70%, 95% and 100% ethanol. Then the cells were denatured using hybridization solution (70% formamide (Sigma Aldrich), 0.5% blocking reagent (Roche, cat. no. 11096176001), 10 mM Tris-HCl (Fisher Scientific) and TelC-Alexa 647 PNA probe (PNA Bio)) for 10 min at 75 °C and incubated in dark for 2 hr at room temperature. After hybridization, cells were washed three times with washing solution (70% formamide and 10 mM Tris-HCl) and three times with PBS. For *MUC4* and *IL6*, cells were incubated with 70% ethanol at 4 °C overnight followed by three washes with PBS. Then the cells were incubated in 0.1 M HCl (Acros Organics) for 5 min at room temperature and washed with 2X saline-sodium citrate (SSC, Sigma Aldrich) twice for 3 min followed by an overnight incubation in 50% formamide diluted in 2X SSC at room temperature. The probes for *MUC4* and *IL6* were human BAC clones (Empire Genomics) covering the gene sequences RP11-436M6-Aqua and RP11-243C6-Aqua, respectively. The probes diluted in the hybridization buffer were added to the cells, denatured at 73 °C for 7 min and incubated for 2 days at 37 °C in a humidified chamber. After hybridization cells were washed with washing solution 1 (0.3% NP-40 (Sigma Aldrich) in 0.4X SSC) at 73 °C for 2 min followed by washing solution 2 (0.1% NP-40 in 2X SSC) at room temperature for 1 min. The cells were imaged in PBS immediately after completion of the FISH. To obtain FISH signal for the cells, for which we recorded H2B-GFP and CRISPR-dCas9-PCP-mCherry signals, we referred to the positions saved in the live cell imaging experiment.

Immunofluorescence staining

Transcription activation was confirmed by immunofluorescent labeling of the transcriptionally active CTD phosphorylated Ser5 RNA Pol II (Abcam, ab5131)[32]. After fixation, cells were permeabilized using 0.2% Triton X-100 (Fisher Scientific) in PBS for 10 min and washed three times with PBS. Next, the cells were incubated in blocking reagent (5% BSA (Sigma Aldrich) in PBS or 10% normal goat serum) for 1 h and then treated with the primary antibody diluted in blocking reagent (1:1000) for 1 h at room temperature followed by a secondary antibody (1:200) (Invitrogen, anti-rabbit Alexa 405, A-31556) for 1 h at room temperature. The cells were washed with PBS three times after each antibody treatment and immediately imaged. It is important to note that colocalization of RNA Pol II foci with PCP-mCherry-labeled sites may be affected by slight shifts during the fixation process, and signal contamination from neighboring active genes. While a signal colocalization is consistent with a gene activation, definitive evidence is achieved by sequence-specific RNA FISH imaging for both *MUC4* and *IL6* (see section *RNA FISH staining*). For measurements of RNA Pol II density across a nucleus, we detected foci within a focal plane by applying a bandpass filter to the measured RNA Pol II signal, which removed the high-frequency noise, followed by detection of puncta whose signal was more than 10% above the bandpass-filtered background signal. The RNA Pol II density was defined as a number of foci normalized by the nuclear area in the given focal plane.

RNA FISH staining

Transcription activation was confirmed by fluorescent labeling of nascent RNA of *IL6* and *MUC4* using RNA FISH. FISH probes were

designed for *IL6* and *MUC4* RNA using the Stellaris RNA-FISH Probe Designer software and purchased from Biosearch Technologies, Inc. We performed hybridization with custom *IL6* or *MUC4* Stellaris RNA FISH Probes labeled with Quasar 670 (Biosearch Technologies, Inc.) in HeLa H2B-GFP cells following the manufacturer's protocol as follows: First, cells were fixed with 3.7% (vol/vol) formaldehyde in PBS (Gibco) at room temperature for 20 min, washed three times with PBS every 5 min, and dehydrated in 70% ethanol at 4 °C for at least 1 hr. Next, cells were treated with Wash Buffer A (20% Stellaris RNA FISH Buffer A (Biosearch Technologies, Inc.), 70% Nuclease-free water, and 10% formamide (Sigma Aldrich) for 5 min at room temperature before incubated in 125 nM probe in hybridization solution (90% Stellaris RNA FISH Hybridization Buffer (Biosearch Technologies, Inc.) in formamide) at 37 °C for 16 hr in a humidified chamber. Then, cells were washed with Wash Buffer A at 37 °C for 30 min and Stellaris RNA FISH Buffer B at room temperature for 5 min. Finally, cells were treated with ProLong Glass Antifade Reagent (Invitrogen) and imaged within 48 hr. All incubation steps were performed in dark. The RNA FISH protocol, which includes fixation and hybridization, can affect the H2B-GFP signal quality in fixed cells, which can appear more diffuse than in live cells[78]. In addition, the images are collected with RNA FISH puncta in focus, so the H2B-GFP signal may appear slightly out of focus due to chromatic aberration[79]. The sequences used to target *MUC4* RNA and *IL6* RNA are listed in Supplementary Tables 8 and 9, respectively.

FISH probe detection

Nuclei with RNA and PNA FISH staining were imaged in 3D, with images collected over all focal planes along the *z*-axis. The detected FISH puncta had intensity well above the background and their positions were detected manually, as the center of each punctum. For puncta co-localization analysis, features found within the same focal plane and <0.5 μm apart were registered as co-localized.

Microscopy and image acquisition

Images were taken with a Yokogawa CSU-X1 spinning-disk confocal head with Spectral Applied Research Borealis modification for increased light throughput and illumination homogeneity and an internal motorized high-speed emission filter wheel on a Nikon Ti-E inverted microscope equipped with a 100x Plan Apo NA 1.4 objective lens and the Perfect Focus System. The microscope was mounted on a vibration-isolation air-table. To image H2B-GFP and CRISPR-dCas9-PCP-mCherry (or Alexa Fluor 546) at the same time, we illuminated the sample simultaneously with two excitation wavelengths, 488 and 561 nm, using two distinct solid-state lasers. The emission was collected with a 405/488/561/640 multibandpass dichroic mirror (Semrock) and separated by the W-View Gemini Image Splitter (Hamamatsu) using the GFP/mCherry dichroic mirror (Chroma Technology), and further passed through ET525/30m and ET630/75m emission filters (Chroma Technology). The two fluorescent signals are allocated to the two halves of the image sensor, producing two distinct images. Images were obtained with a Hamamatsu ORCA-R2 cooled CCD camera controlled with MetaMorph 7 (v. 7.8.9.0, Molecular Devices) software. The pixel size for the 100x objective was 0.065 μm. The observation duration was 20 s with an exposure time of 250 ms. The streams of 16-bit images were saved as multi-tiff stacks. Images were converted to single-tiff images and analyzed using MatLab 2019b - 2023a (The MathWorks). For two-color (red/green) signal registration, we imaged 4 μm TetraSpeck Fluorescent Microspheres (Molecular Probes) and obtained a two-dimensional local transformation matrix[57]. The images were corrected for photobleaching using histogram matching[80]. For FISH probes labeled with the Aqua Dye and for the immunofluorescence secondary antibody labeled with Alexa 405, a 405 nm solid state laser and an ET450/50m emission filter (Chroma Technology) were used. For FISH probes labeled with Alexa 647 or Quasar 670, a 640 nm solid state laser and an ET705/72m emission filter (Chroma Technology) were used.

Single particle tracking

The tracking of labeled genes was carried out using previously published tracking algorithms[57,81] in combination with MatLab analysis (The MathWorks). The preliminary position of the gene locus was first identified manually, then the centroid of the gene locus was computed in each frame as the center of mass for the pixels around the indicated gene locus position. To achieve high precision in tracking, we used previously published algorithms[57] for finding the window, in which the feature is tracked. Such windows are obtained as follows: we filter the photobleach-corrected PCP-mCherry signal in each frame using a tophat filter, then sum the filtered signal over all timeframes and perform watershed on the inverse of the summed signal. Regions too big to correspond to real features are removed, and trajectories estimated from the gene centroid tracking are overlaid. If a trajectory is spanning neighboring windows, these windows are merged. The final window is held fixed for all frames, and the gene centroid is found in every frame from the tophat-filtered, photobleach-corrected signal within this window. This way, we can determine the trajectory of most genes with very high precision and a very low noise floor (~30 nm).

All nuclei were carefully screened for nuclear translation/rotation by assessing the nuclear contours at different time points (Supplementary Figs. 11a, 12b). We find no significant nuclear rotation/translation during our observation time of 20 s. In a rare case that a nucleus does move during our observation time, it is removed from further analysis. We note that the nuclear envelope can exhibit occasional subtle undulations (amplitude ~100 nm)[82](Supplementary Fig. 11b). However, these undulations are only local (Supplementary Fig. 11b–c) and do not present a translation/rotation of the nucleus. All single gene trajectories were corrected for potential nuclear motions by subtracting the centroid motion of the nuclear contour at every frame. Random sites in H2B-GFP signal were identified and matched through I_{ch} and S_{rel} using previously published algorithms[57] and tracked using the procedure described above. The immunofluorescently labeled active RNA pol II foci were detected using previously published algorithm[57].

Displacement Correlation Spectroscopy (DCS)

DCS measures local chromatin displacements simultaneously across the entire nucleus over the entire temporal spectrum of the experiment using H2B-GFP signal in live cells[9]. Displacements are computed using previously published image-correlation-based algorithms[9]. Specifically, the calculation comprises three steps: (*i*) A time series of displacement fields for a time series of fluorescent images is computed using a standard PIV algorithm[83] for all image pairs separated by time lag Δt. (*ii*) The average spatial displacement autocorrelation function (SDACF) is calculated by averaging over all SDACFs calculated for every displacement field obtained in *i* to detect characteristic length scales. (*iii*) Steps *i* and *ii* are repeated for all accessible time lags Δt to obtain temporal evolution of SDACF(Δt), identifying characteristic timescales and length scales in the system. Optionally, a temporal autocorrelation of SDACF(Δt) is performed to characterize the temporal decorrelation in the system.

The displacement fields were computed using the MatPiv 1.60 package[83] (a GNU public license software, http://folk.uio.no/jks/matpiv/index2.html) for MatLab (The MathWorks) in combination with previously described custom-made MatLab routines[9]. The displacement fields were calculated for all time intervals accessible in the experiment, typically 250 ms to 15 s. The resulting displacement fields were filtered using filters "snrfilt", "pkhfilt", and "globfilt" from the MatPiv 1.60 package, evaluating signal-to-noise ratio, peak height of correlation functions, and global velocity distribution to remove spurious vectors.

To obtain DCS maps, we record streams of images over 20 s at an exposure time of 250 ms and compute displacement fields $\mathbf{d}(\mathbf{r}, \Delta t)$ with interrogation windows of $0.26\,\mu m \times 0.26\,\mu m$ for $\Delta t = 0.25$–15 s. At these timescales, nuclear motion was shown to be negligible (<20 nm, see Supplementary Fig. 12e) and does not affect the DCS measurements (Supplementary Fig. 12c–d), which have a noise floor ~40 nm. To assess the extent of coherent chromatin motions, we computed the spatial displacement autocorrelation function $C_{d_x}(\Delta\mathbf{r},\Delta t) = \langle d_x(\mathbf{r},\Delta t) \cdot d_x(\mathbf{r}+\Delta\mathbf{r},\Delta t)\rangle$. DCS maps and $C_{d_x}(\Delta\mathbf{r},\Delta t)$ were computed for 78 nuclei, following procedures described earlier[9]. The correlation score S_c was calculated by identifying the chromatin displacement vectors within distance $\Delta r = 0.13\,\mu m$ around the labeled gene and then calculating the scalar product between the displacements of the gene and the surrounding chromatin ($S_c = \langle \mathbf{d}_g(t)/d_g(t) \cdot \mathbf{d}_{ch}(\mathbf{r}, \Delta t)/d_{ch}(\mathbf{r}, \Delta t)\rangle$) as a function of the distance from the gene center. All DCS calculations were performed in MatLab on New York University High Performance Computing cluster.

Statistics and reproducibility

The statistical significance of results was evaluated by computing p-values using the one-sided χ^2-test for comparing ensemble-averaged *MSD, MSND* and S_c, and the two-sided Student t-test for comparing probability distributions (Supplementary Data 1). Error bars shown in ensemble-averaged curves represent the standard error, error bars provided for fitting parameters represent fitting errors. Sample size was not predetermined. The experiments were repeated until a statistically significant result could be obtained. No data were excluded. Experiments were repeated in 2-3 biological replicates.

Reporting summary

Further information on research design is available in the Nature Portfolio Reporting Summary linked to this article.

Data availability

All data generated in this study are available within the article, Supplementary Information or Source Data file. Source data are provided with this paper.

Code availability

Data analysis code is provided with this paper as Supplementary Data 1.

References

1. Crick, F. H. On protein synthesis. *Symp. Soc. Exp. Biol.* **12**, 138–63 (1958).
2. Crick, F. H. Central dogma of molecular biology. *Nature* **227**, 561–563 (1970).
3. Dekker, J., Marti-Renom, M. A. & Mirny, L. A. Exploring the three-dimensional organization of genomes: Interpreting chromatin interaction data. *Nat. Rev. Genet.* **14**, 390–403 (2013).
4. Gibcus, J. H. & Dekker, J. The hierarchy of the 3D genome. *Mol. Cell* **49**, 773–782 (2013).
5. Bonev, B. & Cavalli, G. Organization and function of the 3D genome. *Nat. Rev. Genet.* **17**, 661–678 (2016).
6. Hübner, M. R. & Spector, D. L. Chromatin dynamics. *Annu. Rev. Biophys.* **39**, 471–489 (2010).
7. Bickmore, W. A. & van Steensel, B. Genome architecture: domain organization of interphase chromosomes. *Cell* **152**, 1270–1284 (2013).
8. Sazer, S. & Schiessel, H. The biology and polymer physics underlying large-scale chromosome organization. *Traffic* **19**, 87–104 (2018).
9. Zidovska, A., Weitz, D. A. & Mitchison, T. J. Micron-scale coherence in interphase chromatin dynamics. *Proc. Natl. Acad. Sci. USA.* **110**, 15555–15560 (2013).
10. Marshall, W. et al. Interphase chromosomes undergo constrained diffusional motion in living cells. *Curr. Biol.* **7**, 930–939 (1997).
11. Belmont, A. S. & Straight, A. F. In vivo visualization of chromosomes using *lac* operator-repressor binding. *Trends Cell Biol.* **8**, 121–4 (1998).
12. Levi, V., Ruan, Q., Plutz, M., Belmont, A. S. & Gratton, E. Chromatin dynamics in interphase cells revealed by tracking in a two-photon excitation microscope. *Biophys. J.* **89**, 4275–4285 (2005).
13. Chuang, C.-H. et al. Long-range directional movement of an interphase chromosome site. *Curr. Biol.* **16**, 825–831 (2006).
14. Chen, B. et al. Dynamic imaging of genomic loci in living human cells by an optimized CRISPR/Cas system. *Cell* **155**, 1479–1491 (2013).
15. Lampo, T. J., Kennard, A. S. & Spakowitz, A. J. Physical modeling of dynamic coupling between chromosomal loci. *Biophys. J.* **110**, 338–347 (2016).
16. Germier, T. et al. Real-time imaging of a single gene reveals transcription-initiated local confinement. *Biophys. J.* **113**, 1383–1394 (2017).
17. Amitai, A. & Holcman, D. Encounter times of chromatin loci influenced by polymer decondensation. *Phys. Rev. E* **97**, 032417 (2018).
18. Khanna, N., Zhang, Y., Dudko, J. S. L. O. K. & Murre, C. Chromosome dynamics near the sol-gel phase transition dictate the timing of remote genomic interactions. *Nat. Commun.* **10**, 2771 (2019).
19. Branco, M. R. & Pombo, A. Intermingling of chromosome territories in interphase suggests role in translocations and transcription-dependent associations. *PLoS Biol.* **4**, e138 (2006).
20. Cavalli, G. & Misteli, T. Functional implications of genome topology. *Nat. Struct. Mol. Biol.* **20**, 290–299 (2013).
21. Zhou, C. Y., Johnson, S. L., Gamarra, N. I. & Narlikar, G. J. Mechanisms of ATP-dependent chromatin remodeling motors. *Annu. Rev. Biophys.* **45**, 153–81 (2016).
22. Shaban, H. A., Barth, R. & Bystricky, K. Formation of correlated chromatin domains at nanoscale dynamic resolution during transcription. *Nucleic Acids Res.* **46**, e77 (2018).
23. Bruinsma, R., Grosberg, A. Y. & Zidovska, A. Chromatin hydrodynamics. *Biophys. J.* **106**, 1871–1881 (2014).
24. Saintillan, D., Shelley, M. J. & Zidovska, A. Extensile motor activity drives coherent motions in a model of interphase chromatin. *Proc. Natl. Acad. Sci. USA.* **115**, 11442–11447 (2018).
25. Pierro, M. D., Potoyan, D. A., Wolynes, P. G. & Onuchic, J. N. Anomalous diffusion, spatial coherence, and viscoelasticity from the energy landscape of human chromosomes. *Proc. Natl. Acad. Sci. USA.* **115**, 7753–7758 (2018).
26. Shi, G., Liu, L., Hyeon, C. & Thirumalai, D. Interphase human chromosome exhibits out of equilibrium glassy dynamics. *Nat. Commun.* **9**, 3161 (2018).
27. Liu, L., Thirumalai, G. S. D. & Hyeon, C. Chain organization of human interphase chromosome determines the spatiotemporal dynamics of chromatin loci. *PLoS Comput. Biol.* **14**, e1006617 (2018).
28. Alberts, B. et al. *Molecular Biology of the Cell* Vol. 35 (Garland Science, 2014).
29. Pombo, A. et al. Regional specialization in human nuclei: visualization of discrete sites of transcription by RNA polymerase III. *EMBO J.* **18**, 2241–2253 (1999).
30. The ENCODE Project Consortium. An integrated encyclopedia of DNA elements in the human genome. *Nature* **489**, 57–74 (2012).
31. Thul, P. J. et al. A subcellular map of the human proteome. *Science* **356**, eaal3321 (2017).
32. Sinha, D. K., Banerjee, B., Maharana, S. & Shivashankar, G. Probing the dynamic organization of transcription compartments and gene loci within the nucleus of living cells. *Biophys. J.* **95**, 5432–5438 (2008).
33. Ochiai, H., Sugawara, T. & Yamamoto, T. Simultaneous live imaging of the transcription and nuclear position of specific genes. *Nucleic Acids Res.* **43**, e127 (2015).

34. Chen, H. et al. Dynamic interplay between enhancer-promoter topology and gene activity. *Nat. Genet.* **50**, 1296–1303 (2018).
35. Gu, B. et al. Transcription-coupled changes in nuclear mobility of mammalian cis-regulatory elements. *Science* **359**, 1050–1055 (2018).
36. Wang, Y., Maharana, S., Wang, M. D. & Shivashankar, G. V. Super-resolution microscopy reveals decondensed chromatin structure at transcription sites. *Sci. Rep.* **4**, 4477 (2014).
37. Hausnerová, V. V. & Lanctôt, C. Chromatin decondensation is accompanied by a transient increase in transcriptional output. *Biol. Cell* **109**, 65–79 (2016).
38. Nagashima, R. et al. Single nucleosome imaging reveals loose genome chromatin networks via active RNA polymerase II. *J. Cell Biol.* **218**, 1511–1530 (2019).
39. Eshghi, I., Eaton, J. A. & Zidovska, A. Interphase chromatin undergoes a local sol-gel transition upon cell differentiation. *Phys. Rev. Lett.* **126**, 228101 (2021).
40. Lee, T. I. & Young, R. A. Transcriptional regulation and its misregulation in disease. *Cell* **152**, 1237–1251 (2014).
41. Misteli, T. Higher-order genome organization in human disease. *Cold Spring Harb. Perspect. Biol.* **2**, a000794 (2010).
42. Fu, Y. et al. CRISPR-dCas9 and sgRNA scaffolds enable dual-colour live imaging of satellite sequences and repeat-enriched individual loci. *Nat. Commun.* **7**, 11707 (2016).
43. Hollingsworth, M. A. & Swanson, B. J. Mucins in cancer: protection and control of the cell surface. *Nat. Rev. Cancer* **4**, 45–60 (2004).
44. Tanaka, T., Narazaki, M. & Kishimoto, T. IL-6 in inflammation, immunity, and disease. *Cold Spring Harb. Perspect. Biol.* **6**, a016295 (2014).
45. Gabay, C. Interleukin-6 and chronic inflammation. *Arthritis Res. Ther.* **8**, S3 (2006).
46. Chapela, P. J., Broaddus, R. R., Hawkins, S. M., Lessey, B. A. & Carson, D. D. Cytokine stimulation of MUC4 expression in human female reproductive tissue carcinoma cell lines and endometrial cancer. *J. Cell Biochem.* **116**, 2649–2657 (2015).
47. Libermann, T. A. & Baltimore, D. Activation of interleukin-6 gene expression through the NF-κB transcription factor. *Mol. Cell Biol.* **10**, 2327–2334 (1990).
48. Zhang, Y., Broser, M. & Rom, W. N. Activation of the interleukin 6 gene by mycobacterium tuberculosis or lipopolysaccharide is mediated by nuclear factors NF-IL6 and NF-κB. *Proc. Natl. Acad. Sci. USA.* **91**, 2225–2229 (1994).
49. Orjalo, A. V. & Johansson, H. E. Stellaris® RNA fluorescence in situ hybridization for the simultaneous detection of immature and mature long noncoding RNAs in adherent cells. *Methods Mol. Biol.* **1402**, 119–134 (2016).
50. Fritzsch, C. et al. Estrogen-dependent control and cell-to-cell variability of transcriptional bursting. *Mol. Syst. Biol.* **14**, e7678 (2018).
51. Rodriguez, J. et al. Intrinsic dynamics of a human gene reveal the basis of expression heterogeneity. *Cell* **176**, 213–226 (2019).
52. Landry, J. J. et al. The genomic and transcriptomic landscape of a HeLa cell line. *G3 Genes Genomes Genet.* **3**, 1213–1224 (2013).
53. Alpert, T., Herzel, L. & Neugebauer, K. M. Perfect timing: splicing and transcription rates in living cells. *Wiley Interdiscip. Rev. RNA* **8**, e1401 (2017).
54. Han, J., Xiong, J., Wang, D. & Fu, X.-D. Pre-mRNA splicing: where and when in the nucleus. *Trends Cell Biol.* **21**, 336–343 (2011).
55. Raj, A. & Van Oudenaarden, A. Nature, nurture, or chance: stochastic gene expression and its consequences. *Cell* **135**, 216–226 (2008).
56. Sharif, O., Bolshakov, V. N., Raines, S., Newham, P. & Perkins, N. D. Transcriptional profiling of the LPS induced NF-κB response in macrophages. *BMC Immunol.* **8**, 1–17 (2007).
57. Eaton, J. A. & Zidovska, A. Structural and dynamical signatures of local DNA damage in live cells. *Biophys. J.* **118**, 2168–2180 (2020).
58. Annibale, P. & Gratton, E. Single cell visualization of transcription kinetics variance of highly mobile identical genes using 3D nanoimaging. *Sci. Rep.* **5**, 9258 (2015).
59. Qin, P. et al. Live cell imaging of low- and non-repetitive chromosome loci using CRISPR-Cas9. *Nat. Commun.* **8**, 14725 (2017).
60. Kimura, H. & Cook, P. R. Kinetics of core histones in living human cells: little exchange of H3 and H4 and some rapid exchange of H2B. *J. Cell Biol.* **153**, 1341–1354 (2001).
61. Miron, E. et al. Chromatin arranges in chains of mesoscale domains with nanoscale functional topography independent of cohesin. *Sci. Adv.* **6**, eaba8811 (2020).
62. Zidovska, A. The rich inner life of the cell nucleus: dynamic organization, active flows, and emergent rheology. *Biophys. Rev.* **12**, 1093–1106 (2020).
63. Leidescher, S. et al. Spatial organization of transcribed eukaryotic genes. *Nat. Cell Biol.* **24**, 327–339 (2022).
64. Eshghi, I., Zidovska, A. & Grosberg, A. Y. Symmetry-based classification of forces driving chromatin dynamics. *Soft Matter* **18**, 8134–8146 (2022).
65. Mahajan, A., Yan, W., Zidovska, A., Saintillan, D. & Shelley, M. J. Euchromatin activity enhances segregation and compaction of heterochromatin in the cell nucleus. *Phys. Rev. X* **12**, 041033 (2022).
66. Zidovska, A. The self-stirred genome: large-scale chromatin dynamics, its biophysical origins and implications. *Curr. Opin. Gen. Dev.* **61**, 83–90 (2020).
67. Eshghi, I., Zidovska, A. & Grosberg, A. Y. Activity-driven phase transition causes coherent flows of chromatin. *Phys. Rev. Lett.* **131**, 048401 (2023).
68. Eshghi, I., Zidovska, A. & Grosberg, A. Y. Model chromatin flows: numerical analysis of linear and nonlinear hydrodynamics inside a sphere. *Eur. Phys. J. E.* **46**, 69 (2023).
69. Saintillan, D. & Shelley, M. J. Emergence of coherent structures and large-scale flows in motile suspensions. *J. R. Soc. Interface* **9**, 571–585 (2012).
70. Saintillan, D. & Shelley, M. J. Instabilities and pattern formation in active particle suspensions: kinetic theory and continuum simulations. *Phys. Rev. Lett.* **100**, 178103 (2008).
71. Manna, R. K. & Kumar, P. S. Emergent topological phenomena in active polymeric fluids. *Soft Matter* **15**, 477–486 (2019).
72. Laghmach, R., Di Pierro, M. & Potoyan, D. A. The interplay of chromatin phase separation and lamina interactions in nuclear organization. *Biophys. J.* **120**, 5005–5017 (2021).
73. Jiang, Z., Qi, Y., Kamat, K. & Zhang, B. Phase separation and correlated motions in motorized genome. *J. Phys. Chem. B* **126**, 5619–5628 (2022).
74. De Gennes, P.-G. *Scaling Concepts in Polymer Physics* (Cornell University Press, 1979).
75. Doi, M. & Edwards, S. F. *The Theory of Polymer Dynamics* (Oxford University Press, 1988).
76. Rubinstein, M. & Colby, R. H. *Polymer Physics* (Oxford University Press, 2003).
77. Benchling. *CRISPR Guide RNA Design*. https://benchling.com/crispr (2024).
78. Sakhalkar, H., Dewhirst, M., Oliver, T., Cao, Y. & Oldham, M. Functional imaging in bulk tissue specimens using optical emission tomography: fluorescence preservation during optical clearing. *Phys. Med. Biol.* **52**, 2035 (2007).
79. Pawley, J. *Handbook of Biological Confocal Microscopy*, 3rd ed. 2006 edn, Vol. 986 (Springer-Verlag New York Inc, 2006).
80. Cox, I. J., Roy, S. & Hingorani, S. L. Dynamic histogram warping of image pairs for constant image brightness. *In Proc. IEEE Image Process.* **2**, 366–369 (1995).

81. Crocker, J. C. & Grier, D. G. Methods of digital video microscopy for colloidal studies. *J. Colloid Interface Sci.* **179**, 298–310 (1996).
82. Chu, F.-Y., Haley, S. C. & Zidovska, A. On the origin of shape fluctuations of the cell nucleus. *Proc. Natl. Acad. Sci. USA.* **114**, 10338–10343 (2017).
83. Sveen. & Kristian, J. *An Introduction to Matpiv v. 1.6. 1.* https://www.duo.uio.no/handle/10852/10196?locale-attribute=no (2004).

Acknowledgements

We thank Jane Skok, Pedro Rocha and Yi Fu for the CRISPR plasmid constructs. We thank Jonah Eaton and Rong Zheng for help with random sites tracking and the FISH protocol, respectively. DCS calculations were carried out using New York University High Performance Computing cluster. This research was supported by the National Institutes of Health Grants R00-GM104152 (A.Z.) and R01-GM145924 (A.Z.), the National Science Foundation Grants CAREER PHY-1554880 (A.Z.), PHY-2210541 (A.Z.) and CMMI-1762506 (A.Z.), and a New York University Whitehead Fellowship for Junior Faculty in Biomedical and Biological Sciences (A.Z.).

Author contributions

A.Z. designed research; F.-Y.C., A.S.C., S.L. and A.Z. performed research; F.-Y.C., A.S.C., S.L. and A.Z. contributed new reagents/analytic tools; F.-Y.C., A.S.C., S.L. and A.Z. analyzed data; and F.-Y.C., A.S.C., S.L. and A.Z. wrote the paper.

Competing interests

The authors declare no competing interests.

Additional information

Supplementary information The online version contains supplementary material available at https://doi.org/10.1038/s41467-024-51149-4.

Correspondence and requests for materials should be addressed to Alexandra Zidovska.

Peer review information *Nature Communications* thanks Kerry Bloom, Kerstin Bystricky, Hiroshi Ochiai and the other, anonymous, reviewer(s) for their contribution to the peer review of this work. A peer review file is available.